Ultrasonic Power Transfer for Ultra-High-Frequency Biphasic Electrical Neural Stimulation

Lucia Tacchetti

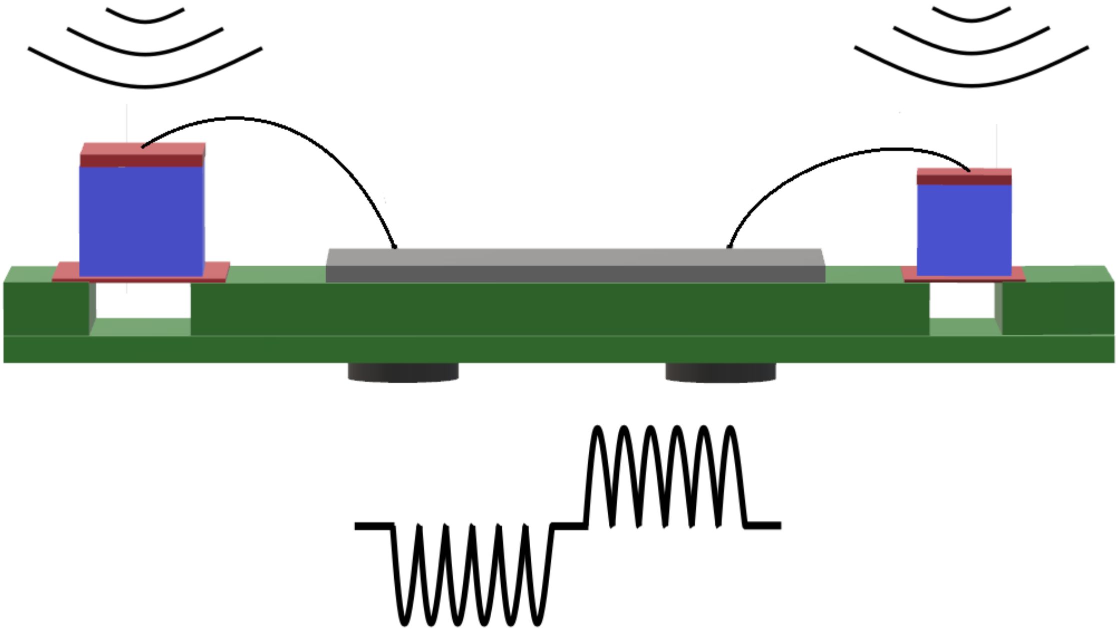

Ultrasonic Power Transfer for Ultra-High-Frequency Biphasic Electrical Neural Stimulation

By

Lucia Tacchetti

in partial fulfilment of the requirements for the degree of

Master of Science
in Biomedical Engineering
Specialisation: Biomedical Electronics

at the Delft University of Technology,
to be defended publicly on Friday June 15th, 2018 at 10:00 A.M.

Supervisor:	Dr. Vasiliki Giagka	
Thesis committee:	Prof. dr. ir. W. A. Serdijn,	TU Delft
	Prof. dr. ir. R. Dekker,	TU Delft
	Dr. M. Mastrangeli,	TU Delft

This thesis is confidential and cannot be made public until June, 2020.

An electronic version of this thesis is available at http://repository.tudelft.nl/.

Abstract

Neurostimulators have been developed over the past few decades to treat various diseases, such as Parkinson's disease, chronic pain, epilepsy, migraine and bladder dysfunction. One of the major design challenges is the selection of a powering method that could supply mW power levels to miniaturized implanted devices. Among several methods, wireless power transfer is often used to directly supply the electronics or to recharge an implanted battery. In particular, the interest in ultrasonic waves as source of power and data for implantable medical devices has recently grown, particularly due to the advantages over RF and inductive coupling power transfer. In fact, ultrasounds can deliver higher power to mm-sized and deeply (> 10 cm) implanted receivers than the other techniques. Moreover, acoustic waves do not interfere with electromagnetic fields.

Conventionally, biphasic constant current or constant voltage pulses are selected for stimulating nerve tissue. The first (usually cathodic) phase has the purpose of activating the excitable nerve fibres, while the second (usually anodic) phase reverses the direction of the stimulation current to avoid long-term accumulation of charge. Alternatively, Ultra-High-Frequency stimulation can be employed. This consists of current or voltage pulses at a high frequency (≥ 1 MHz), which are obtained from a DC source and the operation of high-frequency switches. In both techniques, when a wireless supply is chosen, the received AC signal is rectified, stored and regulated to operate the usually low-voltage blocks of the rest of the system. Nonetheless, up-conversion of the signal is often required to provide enough voltage compliance to operate an output stage connected to the stimulating electrodes.

Taking a more radical approach, it is possible to avoid the lossy conversion from AC to regulated DC and from that to high-frequency stimulation by eliminating the need of power storage, regulation and up-conversion. To this end, the aim of this work was to design a circuit topology that generates ultra-high-frequency pulses by rectifying the sinusoid obtained from an ultrasound transducer and using the obtained waveform to directly stimulate the tissue in a biphasic fashion. This could result in a highly efficient and miniature circuit, which has the potential to be used for stimulating small peripheral nerves.

Simulations in LTSpice were conducted to analyse the performance of the proposed system. The operation was then verified by measurements with a fabricated prototype, which was capable of providing biphasic pulses by receiving a signal from ultrasound piezoelectric transducers and driving a pair of electrodes.

Acknowledgement

I would like to thank several people for their contribution in this project and for being of valuable help in many aspects of my MSc studies.

Vasso, for guiding me through all the steps of this long project and teaching me what good research is. Your experience and passion are inspiring. You were always confident in my potential; this helped me to never give up. I hope our paths will cross again in future.

Wouter, for sharing his knowledge and giving precious hints at crucial points of the project. It was a pleasure to work in your group and to get motivated thanks to your enthusiasm.

Ali, for his help with the PCB fabrication and the technical advice during measurements.

People from the department of Imaging Physics, in particular Verya for providing the ultrasound transducers and helping to get a deeper understanding of acoustic theory, and Emile for realizing the setup to use the transducers.

Nikolas from ECTM, for helping with the impedance measurements of the electrodes. Zu-Yao from EI, for helping with the impedance measurements of the piezoelectric transducers. And thanks to all those people in EWI that were willing to answer my questions.

All the people of the Bioelectronics group for being great colleagues and friends. Thank you because I learnt so much from all of you and you have made me feel comfortable carrying on my project in a *gezellig* environment.

All the friends and fellow students in Delft, for making the study load lighter with their company and making me travel the world with their stories and different customs. And thanks to those friends and relatives in Italy that showed interest in what I was doing beyond the Alps.

Makrina and Kostas. You are the best friends I could ask for in the Netherlands. Thank you for the laughter, Greek craziness and kindness, and for the support you gave me during these Dutch years. *Efharistò!*

Jacopo. Thank you for having fun with me in exploring the Netherlands, collecting unforgettable memories, or just for having a break from a stressful week of lectures, exams or thesis. But more importantly, thank you for being there during my darkest moments. You consoled me and patiently helped me seeing the beauty of what I had around and the value of what I had chosen to do. Thank you for always showing me my qualities and never giving up on me.

My sisters. Maria Chiara, thank you for being patient and kind with me. Maddalena, thank you for being an inspiration for opening my mind and knowing other realities and cultures. You both taught me the importance of following my dreams and being passionate in what I do. You are great sisters and strong women and were always sure I could make important things in the field I chose to study: I will not let you down.

My parents. Without your complete support this would have never been possible. You have always believed in me and I am happy I could make you proud. *Grazie mamma e papà* for being there when I needed you, for raising me with love, giving me the interest in science and knowledge, and letting me live this experience.

CONTENTS

List of figures

List of tables

1. Introduction

1.1. Powering an implantable neurostimulator

Neurostimulators have been employed over the past few decades to treat various diseases. From deep-brain and spinal cord, to vagus nerve and sacral nerve stimulation, electrical pulses are applied to the human neural pathways to address conditions such as Parkinson's disease, chronic pain, epilepsy, migraine and bladder dysfunction. The goal is to induce or inhibit action potentials travelling throughout the body, in order to modulate the operation of an organ and/or muscles. This treatment is possible thanks to implanted electronic devices that generate a programmed therapeutic stimulation pattern [1],[2].

Ideally, the implantable neurostimulator will be small enough to target single peripheral nerves or single neurons so that only the desired activity is elicited without side effects caused by the recruitment of nearby nerve fibres. However, this leads to a great design challenge: powering a miniaturized implant. In fact, a neurostimulator will require a power of 100 mW or more to guarantee the right operation of all the electronics, and adequately deliver enough charge to the targeted tissue [2],[3].

This section illustrates three categories of powering methods -storage elements, environmental harvesting, wireless power transfer- for implantable medical devices (IMDs), with the aim of selecting the most suitable one for a small neurostimulator. Special attention will be given to the amount of energy obtainable from each technique and to the size of the required device. Moreover, biocompatibility will be considered in the discussion: the selected method should not harm the body and the surrounding tissue should not hinder the correct operation of the implant.

1.1.1. Storage elements

Energy storage elements are divided into two main groups: batteries and capacitor/supercapacitors. The former group includes both primary (i.e. non-rechargeable) and secondary (i.e. rechargeable) batteries. Capacitors and supercapacitors are briefly illustrated in the second paragraph, and more characteristics can be found in *Table 1*.

Batteries

Lithium (Li) based batteries have been widely used in IMDs as a main source of power for the electronics. Li-anodes provide high energy density (100–300 Wh/Kg) and can be combined with different cathode materials. The most common ones are iodine-polyvinyl pyridine (I_2-PVP), manganese dioxide (MnO_2), carbon monofluoride (CFx), silver vanadium oxide (SVO), and hybrid compositions [3],[4]. These kinds of batteries are non-rechargeable, and thus, used for low-current drain devices, such as pacemakers, which require low power (e.g. 100 µW) and are usually in stand-by operation. For high rate discharge systems (e.g. hearing devices, neurostimulators, and left ventricular assist devices), which require power in the mW range with continuous or frequent discharge, secondary batteries are selected [3]. They are composed by a carbonaceous anode and a metal oxide cathode (e.g. graphite or lithium cobalt oxide) so that the redox-reactions can be reversed by changing the direction of the current through the battery. Secondary batteries shows a higher nominal voltage than non-rechargeable ones, and can be smaller (down to 2 cm^3) [4]. Moreover, flexible and biodegradable batteries are being investigated in order to power implantable microsystems and be integrated on ingestible/injectable and flexible devices [5].

Nuclear batteries have also been used in pacemakers due to their long service life (> 15 years) and the stability of their output energy. In these batteries, radioisotopes carry energy that is then transformed in electricity. However, they expose the human body to high risk of radioactivity and they require large sizes for high output power. For these reasons, they are not considered ideal means of powering implants [6].

Capacitors and supercapacitors

While batteries store their energy in a chemical form, capacitors store it in the electric field between two conductive plates. Capacitors can provide higher power density and faster charge and discharge than batteries. However, their charge storage is limited by the surface area of the capacitive plates. Supercapacitors can fill the gap between the other two storage elements by providing higher power than batteries in the same volume and still having higher energy density than capacitors. They store energy in the charges building at the two sides of an ion-permeable insulator, which is inserted in the electrolyte. They are mainly suitable for high-power, fast-discharge applications and have a higher capacitance than conventional capacitors. However, they can only withstand lower voltages (2.3-2.75 V) [7],[8].

1.1.2. ENVIRONMENTAL HARVESTING

In this subsection, methods to harvest power from the body environment are explained in four main paragraphs: biofuel cells, thermoelectricity, vibrations harvesting, and other mechanisms. More properties for each technique are reported in *Table 2*.

Biofuel Cells

In a biofuel cell, oxidation of the fuel (e.g. glucose, harvested from the body environment) occurring at the anode by means of a catalyst, such as an enzyme or a microorganism, generates electrons; these travel to the cathode via an external circuit, thus forming an electrical current. Protons reach the cathode passing through a proton-selective membrane between the two chambers. Reduction of the oxidant (e.g. oxygen) occurs at the cathode [6]. There exist different types of cells based on the type of catalyst: enzymatic, microbial, and abiotic. Enzyme-based cells give higher energy density at the cost of short lifetime, whereas microbial fuel cells have long-term stability and efficiency, but with a low power density [3]. GBFCs (Glucose Biofuel Cells) were tested for 3 months [9] and 110 days [10] in the abdomen of rats, and for 12 days in their brains [11], giving few µW of output power. An example of an abiotic biofuel cell is reported in [12]; this cell exploits glucose as a fuel from human serum and produces an open circuit voltage of 0.35 V, which is amplified by an energy harvesting circuit to activate a commercial pacemaker. The catalytic electrodes are modified with inorganic nanoparticles.

Thermoelectricity

Temperature gradients within the body can generate a voltage across a thermocouple, usually formed by n-doped and p-doped semiconductors, thanks to the Seebeck effect[a] [6]. Only one research reports an experiment *in vivo*: Yang et al. [13] implanted a thermocouple in a rabbit, obtaining 25 mV of output voltage with 5.7 K of temperature difference. Higher voltages might be reached by cascading multiple thermocouples; however, at the price of a larger system [6].

Vibrations harvesting

Electromagnetic generators. Electric current is generated in a harvesting circuit thanks to the relative motion between a permanent magnet and a coil. Movements within the body displace the magnet causing a variation in the magnetic flux through the coil, and thus, generating an

[a] When two different conductors are joined together at one point and a temperature difference is maintained between the joined and the non-joined parts, an open-circuit voltage will develop between the non-joined parts of this thermocouple [18].

electrical current, which can potentially be used to power an implantable device [3]. Only feasibility studies have been conducted, with few examples *in vivo*. Moreover, data on biocompatibility and long-term operation are not available. Roberts et al. [14] and Goto et al. [15] tested electromagnetic generators as power source for pacemakers in a pig and a dog model, respectively. Power between 40 µW and 200 µW could be achieved by exploiting the motions of the heart.

Electrostatic generators. The relative movement of two capacitive plates due to an external force changes either the voltage across them or the charge; the capacitor works under fixed charge or fixed potential, respectively [16]. An energy source is needed to charge the capacitor before it can be used in a harvesting system [3]. Tashiro et al. [17] developed a variable capacitance-type electrostatic (VCES) generator to drive a cardiac pacemaker by exploiting the ventricular motion of a canine heart; they could harvest a mean power of 36 µW continuously for more than 2 hours.

Piezoelectricity. Different materials, such as gallium arsenide (GaAs) and zinc oxide (ZnO), are electrically polarized when receiving a mechanical stress [18]. Both continuous and discontinuous motions of the human body may be used to generate electrical current in a harvesting circuit: the former movements comprise respiration and blood flow, whereas the latter indicate movements of limbs [6]. Power of 1 W can be generated by a transducer in a shoe heel [6]. *In vivo* testing were performed by Hwang et al. [19], who powered a cardiac pacemaker by exploiting the heart contractions of a living rat. They used lead magnesium niobate–lead titanate (PMN–PT) single-crystal thin film as transducer, reaching an output power of 1.2 mW. Dagdeviren et al. [20] fabricated piezoelectric transducers made of lead zirconate titanate (PZT) for harvesting energy from the mechanical movements of heart, lung, and diaphragm in two animal models, bovine and ovine.

Other mechanisms

Muscle contractions due to external stimulation. If a muscle is stimulated, the energy generated by its contractions can be harvested by an implanted device: part of it will be needed to stimulate the muscle, whereas the power in excess can be used to stimulate the site of interest, such as the heart or a nerve. Sahara et al. [21] shown the feasibility of this concept by stimulating the gastrocnemius muscle of a toad and obtaining exceeding net power of 111 µW. A schematic of their system is shown in *Figure 1*: the electrical energy is generated by a magneto rotor, which is activated by muscle contractions.

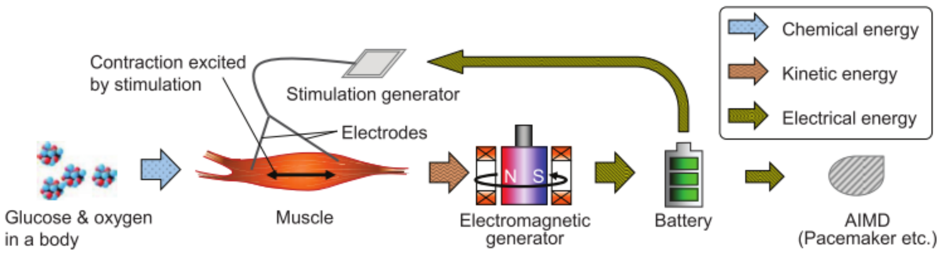

Figure 1. *The linear motion of a stimulated muscle is converted into rotational motion: this allows an electromagnetic generator to charge an active implantable medical device (AIMD) and a stimulator for contracting the muscle* [21].

Skin conduction. A subcutaneous battery can be charged by means of a transcutaneous recharging circuit, which makes use of skin conduction properties. Tang et al. [22] modelled this kind of system as shown in *Figure 2*: when a battery is positioned between two external electrodes (1 and 2 in the figure), electrical current penetrates the skin and flows toward two internal electrodes (3 and 4 in the figure), thus recharging the implanted battery. The authors were able to pass 2.8 mA through the skin of a pig with a 27% of current transmitting efficiency.

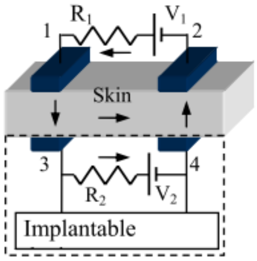

Figure 2. *Model of a transcutaneous battery recharging circuit* [22]. *V_1 and V_2 are the nominal voltages of the external and internal battery, respectively. R_1 and R_2 are the internal resistances of the batteries.*

1.1.3. Wireless power transfer

This subsection illustrates four different methods to wirelessly transfer power from outside the body, through the skin and toward the implant. More details are highlighted in *Table 3*.

Optical Charging

An external laser diode is used to radiate light in the near-infrared (nIR) or infrared region. An implanted photodiode array receives the radiations and converts them into electrical current to recharge an implanted battery or directly power the IMD. The array is composed by numerous photovoltaic (PV) cells (i.e. p-n junctions), which are charged by incident photons and release free electrons [6]. Goto et al. [23] implanted subcutaneously in a rat a photodiode array with the aim of recharging the lithium battery of an implantable device. More recently, Liu et al. [24] tested flexible poly-vinylidene difluoride (PVDF) microbelts implanted subcutaneously in rats to convert irradiated nIR light into voltage/current pulses thanks to the pyroelectric[b] properties of the material; in this way, they were able to directly stimulate the heart of the animal and modulate its beat. In order to keep the receiver small, while avoiding absorption of the irradiations from the tissue, the PV converter should be implanted subcutaneously [24]. In fact, when the tissue is thicker, the size of the receiver must increase to keep the same delivered power (e.g. receiver of 10 cm^2 under 2 mm of human skin against 5.6 cm^2 under 0.8 mm of rat skin) [23]. A way to implant the PV cell deeper in the body, while maintaining the same size and efficiency, is to transmit the incident light to the receiver via an optical fibre, as described in [25]; their system can also work with sunlight, apart from nIR radiations.

Inductive Coupling (near-field)

A current flowing through a primary coil generates a magnetic field that causes a voltage to be induced in a secondary coil, which is inductively coupled to the primary one. The highest efficiency is reached when the two coils are tuned at their resonant frequencies [26]. The operation in the low-megaHertz range is favoured to keep a low tissue absorption of radiations [6]. However, the efficiency of energy transfer not only depends on the operating frequency, but also on the self-inductance of the coils, their distance and alignment, which in turn affect the mutual inductance, thus the coupling between the coils. When the distance between the coils increases and the radius of the coils decreases, the intensity of the magnetic field drops, along with power transfer efficiency. Moreover, larger inductance values would be preferred to increase the quality factor of coils (Q); however, the size of coils is restricted in implantable applications [5]. Ways to improve the power link efficiency have been investigated. As an example, RamRakhyani et al. [27] developed a 4 coils system to deliver energy to an implant by using high Q coils; they showed a power-transfer efficiency of 80% with a decrease efficiency-profile dependency on the coils

[b] Property of materials that produce electric charge as they undergo a temperature change [90].

distance. Moreover, on-chip integrated coils may help in reducing the size of the receiver [28]. Finally, different systems were tested in rat models for powering a muscle stimulator [29], an epidural spinal cord stimulator with EMG recording and bio-impedance measurements [30], and a DBS (Deep Brain Stimulation) system for brain stimulation and recordings using one implanted coil in freely-moving rats [31].

Radiative energy transfer (mid to far field)

In RF (radio-frequency) power transfer, antennas are positioned in the far-field area of the electromagnetic propagating field. The operating frequencies are in the Giga-Hertz range; these transmission frequencies were shown to be optimal for mm-sized antennas [32]; however, the absorption in tissue is higher when compared to radiations generated with inductive coupling, which is using lower frequencies [33]. The RF attenuation in tissue is also higher and the power density drops quickly in the far-field when spreading further away from the source. On the other hand, antennas do not need to be coupled, and the alignment does not have to be as accurate as in inductive coupling. Moreover, one RF external transmitter can power different implanted systems at the same time [33] and transmitter antennas can be implanted to send information of the body interior, such as in the stent-based system for internal cardiac monitoring developed by Chow et al. [34]. Mid-field RF energy transfer can also be used to transmit power to smaller and deeper implants than inductive coupling and with higher efficiency than RF far-field radiations [33]. In the mid-field region, which is about one wavelength distant from the source, energy mainly travels in propagating mode, thus being subjected only to environmental losses and not to exponential decay as in the radiative near-field [35]. Ho et al. [35] exploited this property and developed a powering system using mid-field radiations for deep-microimplants; they could transfer 195 µW and 200 µW to a 2 mm-diameter coil implanted more than 5 cm under tissue on a porcine heart and brain, respectively.

Ultrasounds

Ultrasound waves oscillate at frequencies higher than 20 kHz, thus above the human hearing range. They can be generated by a piezoelectric ultrasonic transducer (PUT) under the application of a voltage at its terminals; the travelling acoustic waves can then be received by another piezoelectric element that, as a result of mechanical deformation, converts them into a voltage, which is harvested to generate electrical power [33]. Even though piezoelectric materials are mainly exploited as transducer elements, capacitive ultrasonic transducers (CUTs) are also used in energy harvesting [6]; in this case, the ultrasonic waves deform a membrane, thus changing the capacitance between the membrane and the electrodes surrounding it. PZT is mainly used to fabricate PUT [26], whereas graphene has been exploited as membrane for CUT [36]. The main advantages of ultrasound energy transfer for implantable devices include: smaller wavelengths than light at the same frequency that allow targeting of smaller devices, and the immunity to electromagnetic fields [6],[37]. Moreover, they show lower attenuation than RF waves, thus reaching a deeper penetration in tissue [26]. However, although high frequencies are desired to shrink the size of the implanted receiver and avoid cavitation[c], an increase in operation frequency leads to an increased attenuation factor and higher pressure, thus with the risk of heating tissue. Therefore, an optimal selection of frequency exist depending on the application and materials used [26]. Ultrasound powering systems have been investigated for transferring energy to IMDs such as optogenetic stimulator [38], drug delivery device [39], and nerve cuff stimulator [40]. Finally, ultrasounds may be used to communicate with implanted systems and receive recorded data of biopotentials, such as in the neural dust ultrasonic system [37]; its operation was proven

[c] Described as the interaction of a sound field with a gas bubble. A microbubble in the body can implode when subjected to high negative amplitude of an ultrasonic wave, giving rise to high local pressure and tissue heating [91].

in vivo in a rat model, whereas the *in vivo* safety of ultrasonic energy transfer was investigated by Radziemski et al. [41].

1.1.4. Selection of a powering method

Even though Li-based batteries have been used as main power source for IMDs, they have a limited life span and occupy the biggest volume of an implant (25–60% of the total size [42]). On the other hand, secondary batteries do not need replacement, thus risks related to frequent explantation surgery could be avoided. However, the size is still an issue and they need a recharging system. Capacitors, and especially supercapacitors, are small elements that can be used for storage. They both may be used to temporarily store energy; however, they cannot be thought as the only means of powering a neurostimulator. Therefore, other methods were illustrated to directly charge the implant or a storage element.

Environmental harvesting is a promising technique. However, vibrations harvesting devices have issues with controllability and size when high output power is needed. On the other hand, biofuel cells and thermocouples can potentially give continuous power, but at the price of low energy levels. For these reasons, wireless power transfer methods have been investigated to find the most suitable one for a neurostimulator.

Optical charging is not suitable for powering a small neurostimulator, since large devices are needed to reach high output power. Therefore, the other three wireless methods were further compared. *Figure 3* shows the regions of operation for ultrasounds (US), inductive coupling (IC), and RF power transfer based on three main characteristics: obtainable output power, size of the implant and depth of implantation. It can be observed that RF gives lower output power compared to the other two, even though the size of the receiver can be small for high implant depths. IC and US may give the same output power. However, for the same power levels, US can reach smaller and deeper implants without electromagnetic interference. Moreover, the FDA (Food and Drug Administration) puts an intensity limit of 7.2 mW/mm^2 for the use of diagnostic ultrasounds [43], which is much higher than the limit set for the use of RF in the human body (10-100 µW/mm^2) [44]. For these reasons, ultrasonic energy transfer was selected as the most suitable method for powering a mm-sized neurostimulator deeply implanted in the body.

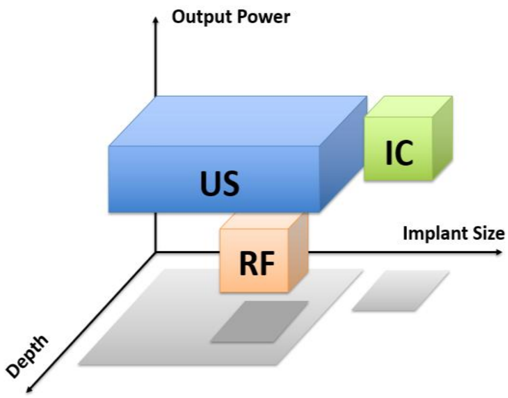

Figure 3. *Regions of operation of three wireless powering methods: ultrasounds (US), inductive coupling (IC), and RF (modified from [44]).*

Table 1. Energy storage elements

	Primary battery	**Secondary battery**	**Nuclear battery**	**Capacitor**	**Supercapacitor**
Storage mechanism	Anode and cathode separated by electrolyte. Irreversible redox reactions occurring at the electrodes to generate a current [3].	Anode and cathode separated by electrolyte. Reversible reactions: during recharge the load is replaced by an electrical source [3].	Energy carried in particles emitted by radioisotope materials [3].	Conductive plates separated by a dielectric. Energy stored in the electric field [3].	<u>EDLC (Electric Double Layer Capacitor):</u> charge stored in a double layer at the electrode-electrolyte interface at both sides of a central insulator. <u>Pseudocapacitor:</u> fast and reversible redox reactions at the electrode surface. <u>Hybrid</u>: one capacitive/pseudocapacitive electrode combined with a battery electrode [3].
Specific energy (Wh/Kg)	100-500 [3]	50-200 [3]	> 20000 [48]	< 0.1 [7]	1-10 [7]
Specific power (W/Kg)	< 1000 [7]	< 1000 [7]	< 100 [48]	>> 10000 [7]	500-10000 [7]
Lifespan: non-rechargeable. Number of cycles and discharge time: rechargeable.	Up to 10 years in low-power pacemaker applications [3].	About 1000 cycles, up to 3 hours discharge time [7]. For a device working 1 hour/day, this corresponds to a lifespan of up to 8.2 years.	>15 years in one pacemaker device [6].	Almost infinite cycle-life, but fast discharge time (10^{-6} to 10^{-3} s) [7].	> 500000 cycles and seconds to minutes of discharge time [7].
Size	Large form factor [45]: 5-10 cm^3 [42].	Large form factor [45]. Down to 2cm^3 [50].	Large form factor [45]. Betacel® battery: 1.8 cm^3 [49]	Small form factor [45].	Small to large form factor[45].
Use in IMDs	Cardiac Pacemakers, cardioverter-defibrillator [6], responsive neurostimulator [51].	Hearing devices, neurostimulators, high energy cardiac implants [3].	Pacemaker [6].	General charge storage. Burst discharge [3].	Power supply for biomedical devices [46] and miniaturized implants [47]. Applications where power burst are needed [7].

Table 2. Environmental harvesting

	Biofuel cell	Thermoelectricity	Electromagnetic generator	Electrostatic generator	Piezoelectricity
Use in IMDs	Only potential uses[d] [52]: -self-powering glucose sensing for diabetics -cardiac pacemaker -drug delivery systems -brain-machine interface [53].	Wearable electronics [3]. Potentially[d], for low power implanted electronics [13].	Wearable applications [16]. Powering of a cardiac pacemaker [14],[15].	Low-power implantable biosensors [16]. Potential[d]self-powered cardiac pacemaker [17].	Wearable applications (ankle, knee, hip, elbow, foot and shoulder) [6]. Potential[d] self-powered cardiac pacemaker [19].
Source of power	Fuel can be taken from body fluids [6].	Presence of temperature gradient within the body [6].	Body/organs movements as power source [3].	Body/organs movements as power source [3].	Body/organs movements as power source [3].
Output power	Few µW [33].	Up to 1.5 mW/cm^2 using silicon nanowires [33].	Few hundreds of µW [6].	µW level [6].	Few µW for implanted harvesters [33].
Biocompatibility and size	Potentially[d], highly compatible [9]. Size: few mm^2 [33].	Not proven. Size: few mm^2 [33].	Not proven. Size: few cm^2 [6]	Not proven. Size for implants is not available.	Proven in vitro [20]. Size: few cm^2 [33].
Short/long term application in an implant	Tested only for short-term [3].	Potentially[d], long-term [13].	Not tested.	Potentially[d], long-term [17].	Potentially[d], long-term [19].
Main advantages	Use of elements present in nature; potentially[d], continuous power delivery [6].	Naturally unlimited lifetime [6].	Many available implantable locations in the human body [6].	Possibility of integration of transducer with other microelectronic circuits [6].	High output power when exploiting discontinuous, voluntary human body movements [6].
Limitations and risks	-µW level of power [6]. -Difficulty in maintaining the biocatalyst in operation [6]. -Risk of biofouling [6].	-Low energy efficiency due to low temperature gradients [3]. -Few hundreds of µW with a gradient of 5 K [16].	Challenges in fabrication techniques for miniaturization [6].	-High pre-charging voltage [3]. -High output impedance and voltage limit the available current [6].	-Large size to obtain high output power and limited implantable locations [6]. -Low energy density [5].

[d]Meaning that the specific application and/or property of the method has not been proven yet, but it was suggested.

Table 3. Wireless power transfer

	Optical charging (nIR radiations)	RF	Inductive coupling	Ultrasounds
Use in IMDs	Potential[d] battery-less implanted stimulators [24]. Recharge of an implanted lithium battery [23].	Neural signals recording devices and implantable monitoring systems [33].	Brain recording systems [33]. Cochlear and retinal implants and implantable neuromuscular stimulators [5].	Neural stimulators [33]. Brain-machine interface [33]. Neural recording [37].
Transmitter and operation frequency or wavelength	External laser diode [6]. Between 760 nm and 1500 nm [24].	Transmitting antenna. From 1 to 2.4 GHz [33].	External coil. Low Mega-Hertz range (0.3-30 MHz) [6].	Piezoelectric/capacitive transducer generating acoustic waves at ultrasonic frequencies. Usually around 1MHz or higher; some cases at the low kHz range [26].
Receiver characteristics (type, size, depth)	Type: photodiodes array (pn-junctions) [23] or pyroelectric material (e.g. PVDF [24]). Size: down to 1.5 x 1.5 mm^2 (photovoltaic cell) [54]. Depth: usually subcutaneous [33].	Type: implanted antenna. Size: few mm^2, less than 1 cm^2 [26]. Depth: range 15-50 mm [26].	Type: implanted coil. Size: from 1 to 4 cm^2 [26]. Depth: subcutaneous or 10-30 mm [26], [33].	Type: implanted piezoelectric/capacitive transducer. Size: from few mm^2 to few cm^2; two cases of more than 15 cm^2 [26]. Depth: from 5 mm up to 200 mm [26].
Delivered power	0.7 W/cm^2 (peak of 2.7 mW) [54].	Up to a few hundreds of µW [26], [33].	From few mW, up to 150 mW [16], [26], [33].	From few mW, up to 440 mW [26].
Main advantages	High volumetric energy density [54].	Working at long distance relative to the size of the antenna [26]. Working with multiple devices at the same time [33].	It can be used for high rate data link and power transmission (especially, short communication) [16].	Short wavelengths, thus smaller receiver size [26]. Low attenuation in tissue, thus deep penetration [26]. Not susceptible to electromagnetic interference [26].
Limitations and risks	High dispersive characteristics of nIR in tissue [33]. Raise of skin temperature by 1.4 °C [16].	Low transfer efficiency, thus low harvested power [33].	Large coils and limited distance to avoid efficiency decrease [33]. Limited carrier frequency to avoid tissue absorption [16].	Trade-off between deep penetration and small-wavelengths (i.e. low and high frequency) [6]. Risk of cavitation [6]. Low penetration in bone [33].

1.2. ULTRASONIC POWER TRANSFER: NEURAL RECORDING AND ELECTRICAL STIMULATION

Various IMDs have been developed that use ultrasound transmission as method for powering the electronics as previously discussed. While many designs focus on the optimization of the AC to DC signal conversion circuitry for both powering and communication [55],[56], there are two systems in literature that stand out because of their simple design; power is not stored in the implant and the signal generated by a piezoelectric transducer is directly used for modulating recorded electrophysiological signals [37] or for stimulating peripheral nerves [40]. Both of them were fabricated and tested *in vivo* in a rat.

Ultrasonic neural dust

Neural dust is a system that uses ultrasonic backscattering for receiving information about electrophysiological potentials [37]. Its operation is shown in *Figure 4.* Pulses at 1.85 MHz (V_{TX}) are sent to an implanted piezocrystal receiver. The physiological potential from the nerve (V_{ephys}) is recorded by a pair of electrodes and modulates the gate of a transistor, thus modulating the current through it and the voltage at the terminals of the piezo-element. Therefore, pulses that are reflected back (V_{RX}) are modulated in amplitude and include the information to reconstruct the signal. Neural dust operates with only 0.12 mW transmitted power. Finally, the implant is encapsulated with medical grade UV-curable epoxy and measures roughly 0.8 x 3 x 1 mm.

Ultrasonically powered nerve cuff stimulator

Larson and Towe [40] developed a nerve cuff stimulator, shown in *Figure 5,* which is composed by a piezocrystal receiver, two discrete components, namely a diode for rectification and a capacitor for passive charge balancing, and two electrodes in Platinum Iridium (PtIr). Ultrasonic tone bursts at 1 MHz were sent to the implant through a tissue phantom and rat tissues, and the force of the leg movements was recorded to assess the efficacy of stimulation. The threshold current was reached at the acoustic intensity of 30 mW/cm^2, and saturation current (i.e. maximum twitch force) at 440 mW/cm^2 (4.17% and 61% of FDA allowed intensity, respectively). Despite the right operation of the stimulator *in vivo*, the system presents different issues. Firstly, the charge injected in the tissue is not directly controlled; the delivered current is estimated from previous water tank measurements with a 2.2 kΩ load, during which the stimulator current was recorded for different acoustic intensities. Moreover, the injected charge is not completely reversed when using monophasic stimulation: this can lead to charge accumulating at the electrode-tissue interface, which might quickly damage the electrodes and/or tissue [57]. Furthermore, a DC-blocking capacitor is not an ideal mean of passive charge balancing, because of the unwanted voltage offset generated across the electrodes at each phase [58]. Finally, the rectification provided by a single diode is inefficient compared to a full-wave rectification.

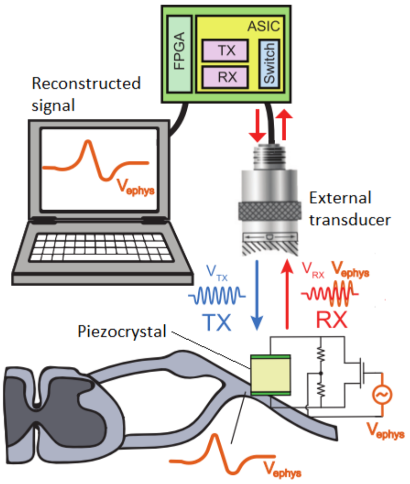

Figure 4. Conceptual drawing of ultrasonic neural dust system (adapted from [37]*).*

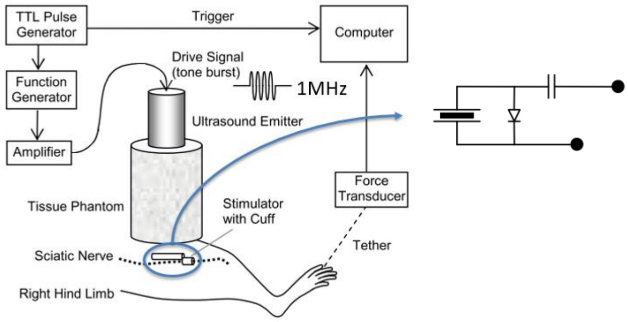

Figure 5. *Drawing of ultrasonically powered nerve cuff stimulator system and detail of stimulator circuitry (adapted from* [40]*).*

1.3. ELECTRICAL NEUROSTIMULATION TECHNIQUES

In conventional constant current (CC) or constant voltage (CV) stimulation, a biphasic pulse is delivered to the tissue. The first (usually cathodic) phase has the purpose to activate the excitable nerve fibres, while the second (usually anodic) phase is needed to completely reverse the injected current and avoid accumulation of charge [57]. In a CC biphasic stimulator (*Figure 6*), the injected charge is regulated by knowing the amplitude (Iamp) and the duration (t) of each phase. Complete charge balancing is then realized by shorting the electrodes after the biphasic pulse [59], or by actively measuring the electrodes voltage after the stimulus and inserting a pulse to cancel the accumulated charge [60]. A basic conceptual schematic of the circuitry providing current controlled stimulation is shown in *Figure 7*. V_{in} is the input voltage that can be obtained either from a battery or from the rectified signal harvested from an external power source. This voltage is generally boosted by a DC-DC converter. The capacitor C is an external component needed to supply the current source, which in turn is controlled by a microcontroller (MCU). Z_{Load} is the impedance seen between the output electrodes.

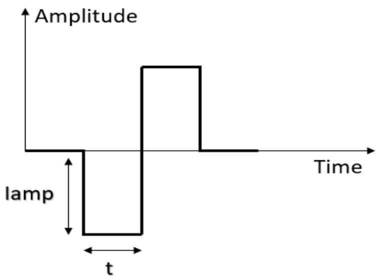

Figure 6*. Biphasic pulse in conventional constant current electrical stimulation.*

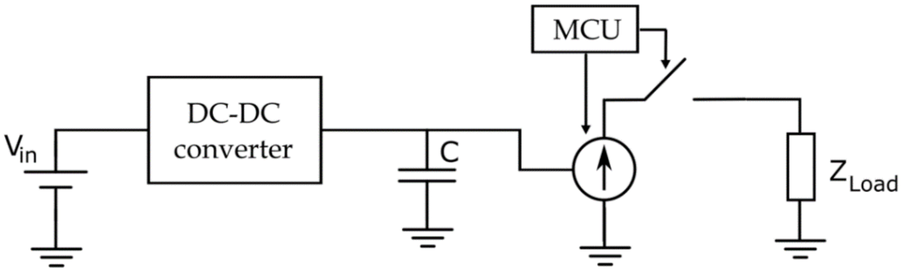

Figure 7. *General architecture of a classical current controlled neural stimulator.*

A different electrical stimulation technique is Ultra-High-Frequency (UHF) stimulation, in which each phase of the biphasic pulse is made up of short pulses at a frequency of 1 MHz or more. This gives the possibility of removing the current source, and thus, the external capacitor. Van Dongen and Serdijn [61] developed a neural stimulator that employs this kind of stimulation principle, showing a higher power-efficiency in multichannel operation than state-of-the-art CC stimulators. The system is shown in *Figure 8*: it requires only one inductor as external component. This is repeatedly charged from V_{in} and then discharged through the load giving a 1 MHz pulsed-shape stimulation waveform. The amount of charge of each high-frequency pulse is defined by regulating the duty cycle signal for the charge and discharge periods. Moreover, the stimulator can handle 16 channels independently and provides active charge balancing after each biphasic pulse.

Van Dongen et al. had previously reported in [62] the efficacy of this stimulation technique in recruiting axons by firstly modelling the response of the nerve fibres and secondly, by testing the UHF excitation *in vitro*. They showed that the Purkinje cells are activated by both constant and UHF current stimulation with the difference that with the latter mode, the capacitive nature of the axon membrane leads to the integration of the exciting pulses, and thus, to a 'staircase' increase of the membrane potential.

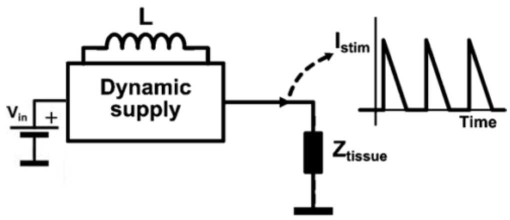

Figure 8*. System architecture of the high-frequency dynamic stimulator proposed in* [61].

1.4. Goal of the project

The DC-DC converter and the current source of a classical constant current stimulator account for the biggest power consumption of the whole system [49],[63]. The UHF stimulation principle improves the overall power efficiency by eliminating the external capacitor and the current source. However, the existing system still needs a high voltage supply (i.e. 20V) for some switches. Moreover, both systems would require a power-management unit for regulating and boosting the energy obtained from a wireless power source. On the contrast, ultrasonic pulses at 1 MHz or more can be used to directly provide UHF electrical excitation of the tissue. In this way, the efficiency advantage of the UHF principle is kept, but with a simplified system architecture that does not require an AC to regulated DC conversion of the input signal for stimulation. As shown before, Larson and Towe [40] already proposed a discrete component system for direct electrical stimulation by harvesting ultrasounds. However, the system is only capable of monophasic stimulation with half-wave rectification of the incoming signal.

The main goal of this project is to provide biphasic UHF electrical neural stimulation by means of ultrasonic power transfer and by keeping a simplified system architecture that does not involve complicated and inefficient power-management. Therefore, this thesis proposes a novel circuit topology that does not require neither power storage nor regulation for supplying active elements of the electronics. Biphasic stimulation is achieved with the operation of five discrete components and one ultrasound transducer for each phase.

The rest of this thesis is organised as follows. Chapter 2 discusses the selected models for the ultrasonic link and electrodes. The details of the proposed topology are presented in Chapter 3, and the performance is verified in simulations in Chapter 4. These are backed up by measurements from a fabricated prototype in Chapter 5. Finally, Chapters 6 and 7 conclude the thesis with a resume of the achievements and future work, respectively.

2. Electrical models

2.1. Ultrasound parameters and models

Ultrasound waves can be characterized by different parameters that will mainly vary based on the material and shape of the transducer. In particular, two main structures of PUT can be found in literature, namely plate and diaphragm. The former operates in bulk-mode, meaning that its lateral sides are fixed and the polarization is in the same direction of the strain (3-3 mode). Whereas, the latter operates in flexure-mode: the poling[e] in the 3-3 axis is perpendicular to the strain, which is predominantly in the 3-1 direction (bending). Both of the structures (*Figure 9)* have one face exposed to the tissue and the other exposed to a backing (e.g. vacuum, air or thick material) [64]. The backing can damp the vibrations of the transducer by absorbing energy from its back face; in this case, a highly dense material, with an acoustic impedance matching the one of the piezo, is used, thus resulting in higher resolution, but lower signal amplitude. On the other hand, when using a backing with different acoustic impedance, such as air, acoustic energy is reflected towards the transducer, which might results in higher signal amplitude or sensitivity, but lower resolution [65].

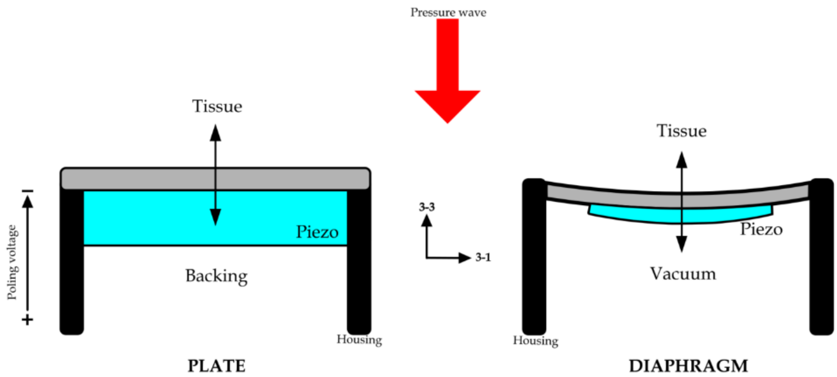

Figure 9. *Two main structures of piezoelectric ultrasound transducers used in implantable devices (modified and adapted from* [64]*). The double arrows represent the direction of vibrations, while the axes orientation is drawn in the middle.*

Christensen D. and Roundy S. [64] modelled and compared the two structures concluding that the diaphragm can generate more power than the plate at the sub-millimetre range and it will be less-sensitive to changes in implantation depth. However, diaphragms work at much lower frequencies than plates of the same thickness. This might be an advantage in some energy harvesting applications where only kHz-frequencies are required. However, for UHF-stimulation, frequencies of 1 MHz or more are selected, and these can be only achieved with plate structures of 1 mm thickness or lower. Moreover, in the millimetre range, the two structures perform similarly and the plate gives a higher mechanical to electrical energy conversion. This is due to the fact that the piezoelectric coupling coefficient in the 3-3 mode, namely k_t or k_{33}, is typically higher (e.g. double or quadruple depending on the material) than the coefficient k_{31} in the 3-1 mode [64].

[e] The poling is a process in which a high voltage is applied to the two opposite faces of the piezo crystal so that the piezoelectric response is defined in a specific direction. Thus, for instance, compression and extension of the plate along the poling axis will result in a voltage with same and opposite polarity as the poling voltage, respectively [92].

Geometries of piezoelectric plate structures

Piezoelectric transducers operating in the 3-3 mode can come in different shapes or geometries as shown in *Figure 10*. Plates (a) and (b) have the lateral dimensions much greater than the thickness, and thus, have the dominant resonance mode naturally in the thickness direction (z-axis), whereas (c) and (d) can have three orthogonal resonance modes coupled to each of the dimensions w, l, and t. The dominant resonant frequency is determined by the dimension that is bigger than the other two [66].

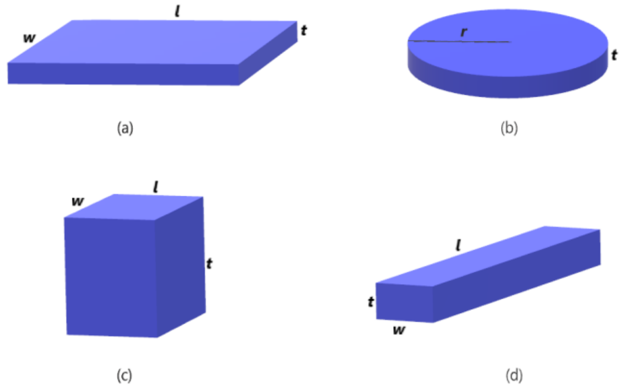

Figure 10. *Plate geometries for vibrations mode along the z axis (modified from* [66]*). (a) Thickness-expander rectangular plate (w,l>>t). (b) Thickness-expander circular plate disk (2r>>t). (c) Length-expander bar (w,l<<t). (d) Width-extensional bar (l>>t,w).*

Chang T. et al. [67] modelled a piezoelectric transducer for IMDs power harvesting applications with the LE (length-expander) mode, as it better approximates small receivers with an aspect ratio (G = l/t) lower than 1. Moreover, the coupling coefficient k_{33}, used for the geometries (c) and (d), is significantly higher than k_t, which is used instead for the thickness-expander plate and disk [64]. For these reasons, a LE geometry was considered when further modelling the piezo-receiver and simulating the final circuit design.

Parameters of piezoelectric transducer

A piezoelectric transducer is characterized by a resonant frequency (f_r), and an anti-resonant frequency (f_a). The maximal response of the transducer to a pressure wave will be observed at its fundamental resonant frequency, which is followed by odd harmonics progressively decreasing in strength. For an aspect ratio G<<1, f_a and f_r can be found with the following equations [68]:

$$f_a = C_f \frac{v}{2t} \tag{1}$$

$$f_r \cong \sqrt{1 - \frac{8k_{33}^2}{\pi^2}} f_a \tag{2}$$

v being the speed of sound in the material, and *t* the thickness of the transducer. C_f is a correction factor needed in the case of a LE-mode transducer with G≤1. The value of C_f will be around 0.7-0.8 [66]. As it can be noticed, the choice of a specific resonant frequency and material for the receiver will determine its dimensions; higher frequencies correspond to thinner transducers. However, selection of higher frequencies also leads to higher pressure attenuation along the wave propagation path, thus reducing ultrasounds penetration in the body and promoting heating of tissue. This effect can be summarized in the formula for the pressure [26]:

$$p(x) = p_0 e^{-\alpha(f)x}, \ \ \alpha(f) = \alpha \times f^k \tag{3}$$

where α(f, k=1) is the attenuation factor of tissue increasing linearly with frequency and p_0 is the pressure at a distance x=0. The value of α is on average 0.54 dB/cmMHz (or 0.062 Np/cmMHz) for soft tissue [69]. Finally, there exists a lower limit for the selection of the operating frequency given by the maximum Mechanical Index (MI) allowed by FDA for diagnostic ultrasounds. The centre frequency f_o of the ultrasound pressure wave should satisfy:

$$MI = \frac{p_n}{f_o} \leq 1.9 \tag{4}$$

with p_n the peak negative pressure of the wave in the body. Higher values of MI give risk of cavitation in the human body [26].

Another important parameter used to characterize a transducer is its acoustic impedance Z_{ac}. This is defined as the product of the density of the material and the speed of sound in the material. The acoustic impedance of PZT is in the order of 30 MRayls, whereas human tissue has an average Z_{ac} of 1.6 MRayls [69]. This impedance mismatch will lead to a high percentage of incident power to be reflected at the interface between the piezo-transducer and the tissue. The ratio between the reflected power and the total incident power can be found with [70]:

$$\frac{P_r}{P_i} = \frac{(Z_2 - Z_1)^2}{(Z_2 + Z_1)^2} \tag{5}$$

with Z_2 the acoustic impedance of the transducer and Z_1 of the tissue, in which the acoustic wave is propagating. With the average values of Z_{ac} for PZT and tissue, (5) results in 0.8; this means that only a 20% of the incident power will be absorbed by the transducer. To overcome this issue, matching layers are designed to be put at the interface between the transducer and tissue. Usually, a quarter wavelength-thick layer with $Z_{ac}=\sqrt{Z_1 Z_2}$ is positioned on the transducer surface to match the impedance. This thickness is chosen to guarantee that the reverberating waves in the matching layer are in phase with the ones generated by the transducer [65]. This layer should be biocompatible and adhere firmly to the transducer. Another technique consists in using multiple layers, which have a total acoustic impedance suitable for matching; this method gives more freedom in the choice of materials [26].

Finally, the sound field of the pressure wave generated by a transducer can be divided into two zones, namely near field and far field, as shown in *Figure 11.* In the near field, the wave is subjected to perturbations having several minima and maxima. Whereas, in the far field, the beam starts to diverge and the wave decays with distance. At distance L from the transducer, called Rayleigh distance, the transition between the two zones is found together with the last maximum of the wave. L can be calculated with equation (6):

$$L = \frac{(D^2 - \lambda^2)}{4\lambda} \tag{6}$$

with λ the wavelength of the pressure wave, and D the aperture width of the transducer [26].

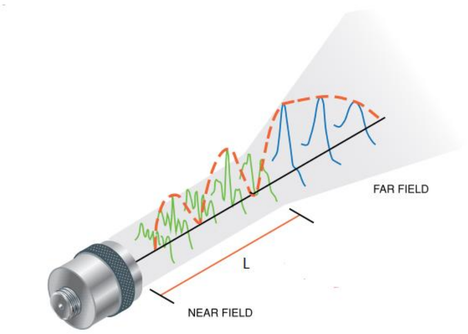

Figure 11. *Illustration of near field and far field for an acoustic beam, with indication of Rayleigh distance L (adapted from* [65]*).*

Lumped elements modelling

An ultrasonic transducer can be modelled with electrical circuit components using the analogy: force-voltage, velocity-current. Therefore, the mechanical pressure caused by the ultrasound waves translates in a voltage across the piezo-transducer, and the current through the electrical circuit is the acoustic particle velocity. Various lumped-elements models were proposed for a one-dimensional analysis of a transducer. The most common equivalent circuit models represent the acoustic wave propagation in a medium as a lossy transmission line. Krimholtz, Leedom, and Matthaei (KLM) [71] developed such a model using a frequency dependent-network and a transformer to couple the electrical port to the mechanical/acoustical ports. Afterwards, Leach [72], and then Püttmer et al. [73] proposed the use of current controlled current sources instead of the transformer. The latter model can be used to simulate an ultrasound transmitter in a Spice simulator [74]. Details about both KLM and Spice lumped-elements models can be found in Appendix A.

Despite the completeness of the aforementioned models, a simpler equivalent circuit can be used for representing the impedance of an ultrasonic transducer around its resonant frequency. This model, known as Butterworth-Van Dyke (BVD), is suitable for a LE-mode transducer and can be seen in *Figure 12(a)* for a piezoelectric receiver. The impedance is modelled as the parallel of a resonant branch (representing mechanical damping R, mass L and elastic compliance C), and a clamped capacitance C_0 [75]. V_{oc} is the open-circuit voltage generated across the piezo-element, when this is not connected to a load. When considering the operation of the receiver at its short-circuit resonant frequency, the simplified model shown in *Figure 12(b)* might be used. In order to model the effect of higher frequency harmonics, extra RLC branches should be put in parallel to the fundamental one [76].

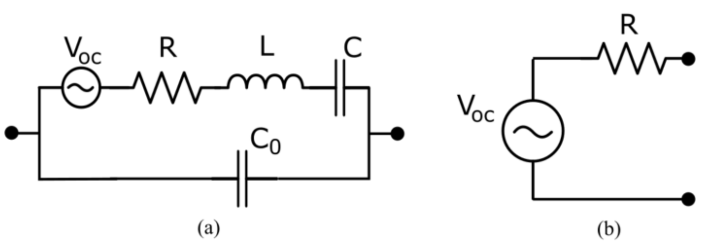

Figure 12*. (a) Modified Butterworth-Van Dyke model for an ultrasonic receiver. (b) Simplified model for operation at short-circuit resonance.*

The values of the parameters of the model can be calculated with following equations [68]:

$$C_0 = \frac{\varepsilon_0 \varepsilon^S A}{t} \tag{7}$$

$$R = \frac{Z_1 + Z_2}{8k_{33}^2 f_r C_0 Z_p} \tag{8}$$

$$C = \frac{8C_0 k_{33}^2}{\pi^2 - 8k_{33}^2} \tag{9}$$

$$L = \frac{1}{4\pi^2 f_r^2 C} \tag{10}$$

ε^S being the dielectric constant under zero strain condition and ε_0 the one of vacuum, A the surface area of the element and t its thickness. Z_1 and Z_2 are the acoustic impedances of the loads at the two faces of the piezo (e.g. tissue and air), and Z_p its acoustic impedance. When considering matching between the piezo electrical impedance and the impedance of the total electrical load, the open-circuit voltage is found as a function of incident acoustic intensity I_{acou} using [38],[68]:

$$V_{oc} = \sqrt{8 \times \eta_{pc} \times I_{acou} \times A \times R} = \sqrt{8 \times P_{av} \times R} \tag{11}$$

with P_{av} the electrical power available at the receiver. The power-conversion efficiency of the piezo (η_{pc}) is the ratio between P_{av} and the incident acoustic power. It depends on the operating frequency, but not on the electrical load and on the transmitter in case of operation in far field [67]. Finally, the -3 dB bandwidth of the transducer can be found with [66],[68]:

$$BW = \frac{1}{Q_e} \cong \frac{4k_{33}^2}{\pi} \frac{Z_p}{Z_1 + Z_2} \tag{12}$$

Q_e being the electrical quality factor.

PZT-5H was chosen as material for modelling piezo-elements in subsequent simulations. However, when designing an ultrasound receiver for a specific application, other materials (e.g. $BaTiO_3$, PMN-PT, PVDF, etc.) might be more suitable depending on their acoustical and electrical impedance. The first selected resonant frequency is 1 MHz in order to comply with the UHF principle and a have a good trade-off between dimensions of the transducer and losses in tissue. *Table 4* reports values of parameters for PZT-5H [66].

Table 4. Properties of PZT-5H.

f_r (MHz)	f_a (MHz)	v (m/s)	k_{33}	$\varepsilon^s/\varepsilon_0$	Z_p (MRayls)
1	1.36	3800	0.75	1470	29

2.2. ELECTRICAL LOAD

Concerning the electrical load of the system, this is defined by the impedance of the stimulating electrodes and their interface with the targeted nerve fibres. Therefore, the load impedance is composed by capacitive and resistive elements as shown in *Figure 13*.

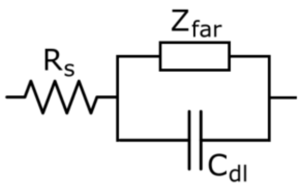

Figure 13. *Electrical circuit model of electrode-tissue interface.*

R_s represents the electrolyte or, more specifically, the tissue ohmic resistance, whereas the parallel of C_{dl} and Z_{far} models the electrode-tissue interface. C_{dl} is the double layer capacitor forming at the interface of the metal electrodes and the electrolyte/tissue, and the Faradaic impedance Z_{far} represents the irreversible reactions occurring at the interface, such as oxidation and reduction [77]. However, when considering polarizable electrodes, used as working electrodes in neural stimulation, the Faradaic impedance shows high values and, therefore, can be neglected in the model. In fact, polarizable electrodes exchange charges with the electrolyte mainly through the capacitive branch, as long as the interface potential is kept within the water window [f] [57]. Furthermore, the charge storage capacity (CSC) of an electrode is another parameter that must be taken into account when deciding the stimulation parameters. The CSC indicates the maximum charge that can be stored reversibly in the electrode.

For determining the magnitude of load impedance, Platinum (Pt) is chosen as material for the electrodes, as it is commonly used in electrical neural stimulation, and has been shown to be biocompatible and resistant to corrosion [57]. Moreover, values for capacitance and resistance of Pt electrodes could be retrieved from relevant papers referenced in this project. The double layer capacitance of a Pt electrode is~ 50µF/cm^2 [78]. Considering the lowest value of CSC for Platinum and an example of maximum charge injected in functional electrical stimulation [79], the minimum area of the electrode would become:

$$\frac{0.2\ \mu C}{50\ \mu C/cm^2} = 0.4\ mm^2$$

And the minimum capacitance would be C_{dl} = 0.2 µF. However, for higher values of CSC (up to 350 µC/cm^2 for Platinum [57]) and for lower injected charge, the area of the electrode can be reduced and C_{dl} can have values lower than 0.1 µF [40]. On the contrary, available electrodes used in electrical stimulation might have larger areas (e.g. 14 mm^2, as in [61]) leading to higher values of C_{dl}, up to 10 µF. Therefore, C_{dl} is taken in the range [100 nF : 10 µF]. Finally, values for R_s range between 200 Ω and 2 kΩ or more, depending on the type of tissue [61],[78].

[f] Electric potential range for safe operation of electrodes that is defined by the reduction of water, forming hydrogen gas, in the negative direction, and the oxidation of water, forming oxygen, in the positive direction [57].

3. System design

After having defined a model for the signal source and the load of the circuit, a system architecture for obtaining biphasic stimulation was designed. Firstly, different features of a standard biphasic neurostimulator were investigated for being adapted to an UHF stimulator powered by ultrasounds. This analysis brought the proposal of a new circuit topology that inverts the direction of the current through the load without requiring power storage and regulation in the system.

3.1. BIPHASIC STIMULATION AND POWER STORAGE

Conventionally, switches in a H-bridge arrangement as in *Figure 14* are used to reverse the direction of the current through the load and thus realizing biphasic stimulation. S_1 and S_3 are closed together during one phase, while S_2 and S_4 are open. The opposite is true in the second phase of the biphasic pulse.

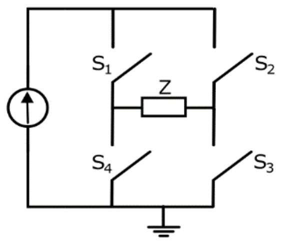

Figure 14. *Switches $S_{1\text{-}4}$ in a H-bridge arrangement across a load Z.*

When using active elements (i.e. MOSFETs) as switches, power supply is necessary. These switches also require the presence of a control unit that decides on their state and regulates the timing. Moreover, data communication might be needed to reprogram stimulation parameters and set the operation of individual channels. Finally, charge balancing is realized passively or actively after each biphasic pulse, as explained in Chapter 1.

An example of a system architecture realizing these features, along with UHF stimulation from an ultrasonic source, is illustrated in *Figure 15*. The sinusoidal signal coming from the electrodes of one or multiple ultrasound transducers is processed through three different paths. In the upper

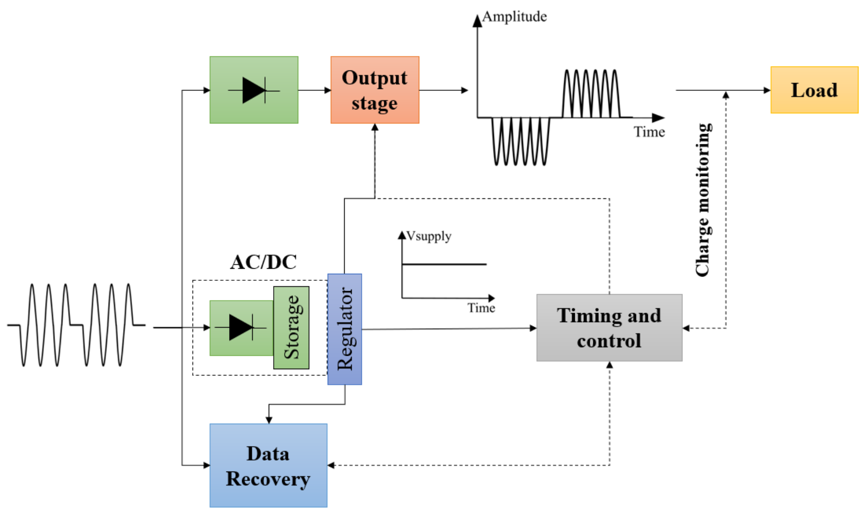

Figure 15. *System architecture for a generic neurostimulator realizing UHF biphasic stimulation and receiving power and data from ultrasound waves.*

path the signal is rectified and directed to the output stage (i.e. H-bridge) for UHF biphasic stimulation of the tissue (load). In the centre, the AC signal is converted to a DC regulated voltage to supply various parts of the system. In the bottom, the signal is demodulated to recover the transmitted data.

Wireless communication

Data can be communicated to the implant by modulating the transmitted ultrasonic waves. Laqua et al. [80] demonstrated the transmission of temperature information from a sensor to a piezoelectric receiver for wireless communication in body area networks (BANs). The transmitted binary data were coded in the length of the 1 MHz ultrasonic burst. A 250 µs and a 750 µs bursts correspond to a logical '0' and a logical '1', respectively. The counter of the receiver microcontroller is triggered by the rising and falling edge of the received bursts. Similarly, Luo et al. [81] used on-off keying with pulse modulation (OOK-PM) for transferring clock and data information to an implanted programmable neural stimulator. Moreover, the signal from the ultrasonic receiver was converted to DC for supplying the stimulator and recharging an internal battery. Recently, Charthad et al. [82] presented a peripheral nerve stimulator powered by ultrasounds. The data for programming the amplitude and pulse width of a CC stimulator are coded in the envelop of the transmitted waves, while the frequency of the stimulation is controlled externally. Furthermore, the harvested signal charges a capacitor, which provides the stimulation current. Finally, data modulation can also be performed at the receiver site and information from the implant can be sent back to the external transmitter with backscattering. This can be achieved by modulating the current through the piezo-receiver as illustrated before (i.e. neural dust recording implant), or by impedance modulation as in [83] and [84]. The latter technique exploits the change of reflection or absorption of the incoming signal by the implanted transducer when loaded with different electrical impedances.

Charge Control

The charge that is being injected in the tissue could be monitored by measuring the voltage (V_c) across a capacitor C in series with the load. The amplitude of V_c will be directly proportional to the charge Q injected in a pulse: $V_c = Q/C$. This will change in time as shown in *Figure 16*.

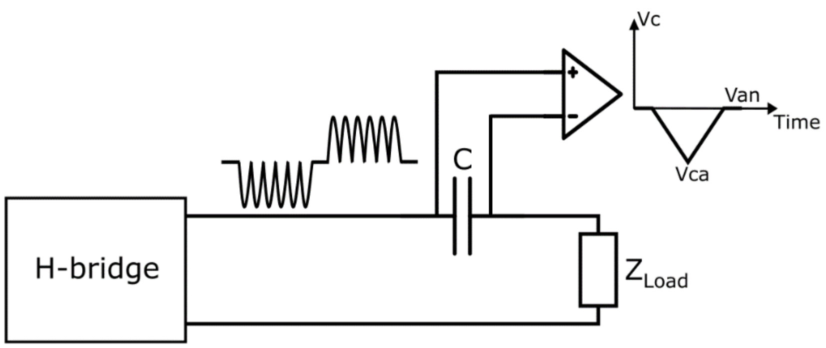

Figure 16. *Monitoring of voltage across a capacitor C in series with a load Z_{Load} during stimulation.*

V_{ca} and V_{an} are the values of V_c after the cathodic and the anodic phase, respectively. For proper charge balancing, V_{an} should be zero meaning that the same charge has been injected in the two phases. Therefore, the second phase should be stopped when V_c increases reaching zero. V_c can be monitored using an OPAMP, which will need a DC power supply, and can be then used to control the state of the switches. The value of C should be as small as possible to minimize the voltage drop across it.

The inserted capacitor could give other advantages apart from charge monitoring. These include: blocking prolonged DC current through the tissue in case of device failure, and faster discharge when shorting the electrodes for passive charge balancing [85]. Nonetheless, if a charge imbalance remains between the two phases and the discharge time t_{dis} is much shorter than the stimulation time, an offset voltage V_{off} across the load is generated and can increase over many stimulation cycles. This can lead to problems for the tissue or the electrodes if V_{off} reaches a threshold triggering irreversible faradaic reactions during t_{dis} between two biphasic pulses. The capacitor C could be discharged separately from the electrodes through a different path after every biphasic pulse, however losing the other advantages. Moreover, when having multiple stimulation channels, a capacitor for each channel is needed, thus leading to an increased device area [58].

3.2. PROPOSED SYSTEM

All the exposed functions for a neurostimulator require the conversion of the ultrasonic signal from AC to a regulated constant supply voltage. On the contrary, in this project, we focused on avoiding this step and any energy losses that come with it. We did so by designing a simple circuit that still provides UHF biphasic stimulation and is novel in operation and architecture when compared to existing neurostimulator powered by ultrasounds.

When harvesting the power from a piezo-element, the electrical signal needs to be rectified to get a net power different from zero at the load. In particular, a bridge rectifier is chosen to obtain full-wave rectification of the sinusoidal input. Two separated bridges might be used to make the current flow through the load in opposite directions for the two phases of the biphasic pulse. *Figure 17(a)* shows how the piezo-receiver P_1 and the bridges should be connected to the load Z to reverse the direction of the current. Switches S_1 and S_2 are closed during the 1st phase, while switches S_3 and S_4 are closed during the 2nd phase. These switches might still require power supply, and they need control for closing and opening during the right phase of the pulse. Another issue of this configuration is that an alternative path is created at each phase of the biphasic stimulation, letting the current flow through the other rectifier (red arrows in *Figure 17(b)*) rather than through the load (blue arrows in *Figure 17(b)*).

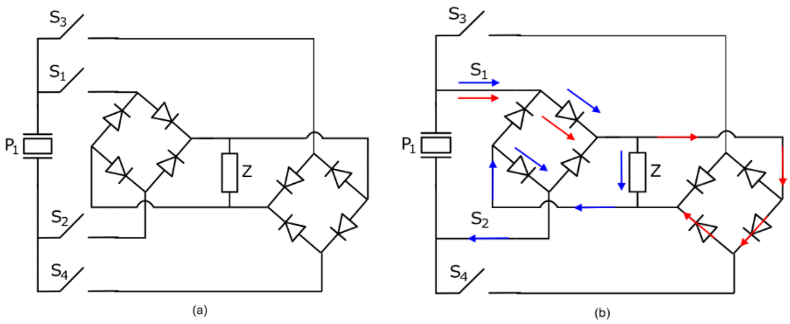

Figure 17. *(a) Piezo P_1 connected with two bridge rectifiers via the switches* S_{1-4}. (b) Example of correct direction of the current (blue arrows) through the load Z during the 1st phase of the biphasic pulse and real direction (red arrows) through an alternative path created by the diodes of the other bridge.

To avoid power storage for operation of the switches before the bridges, the anodic and the cathodic phases are realized with two separated piezoelectric elements having different short-circuit resonant frequencies. Therefore, each of the two phases of the biphasic stimulation pulse is paired with the resonant frequency of one receiver and is generated by sending ultrasounds at that specific frequency. Each of the piezo-receivers is combined with one bridge rectifier and connected to the load as in *Figure 18*. However, in this topology, the current will still flow through the opposite bridge, which creates an alternative path. For this reason, switches must be added after the bridges to assure that the inactive branch is separated from the load during each phase.

3.2. Proposed system

Figure 19 illustrates the switches operation and the direction of the current for different conditions of the input signal.

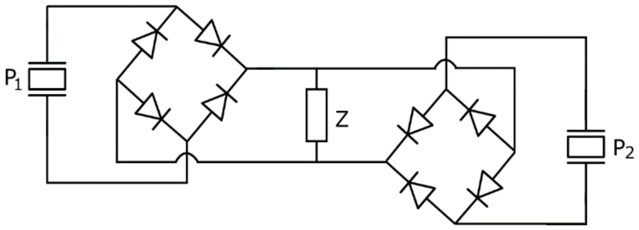

Figure 18. *Circuit configuration with two piezo-elements for biphasic stimulation.*

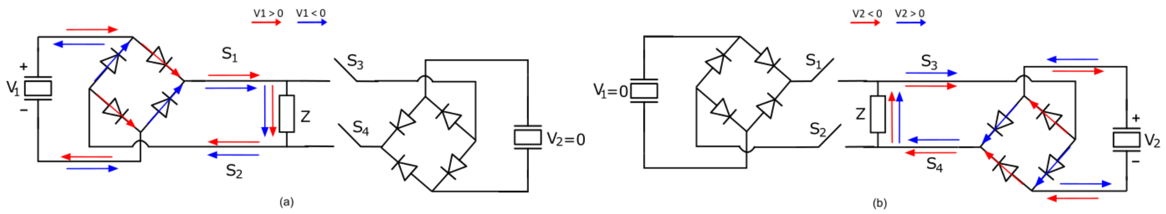

Figure 19. *Operation of the circuit with switches during (a) the 1st phase of a biphasic pulse and (b) the 2nd phase. V_1 and V_2 are the signals generating across the piezo-receivers.*

In order to keep out of the design a dedicated circuit for the supply of the switches and of a control unit, an alternative way of switching had to be found that does not require a power source different from the one available for stimulation.

Firstly, the use of frequency dependent impedances was investigated. Multiresonant passive circuits as in [86] can act as a short-circuit (i.e. low impedance) and as an open-circuit (i.e. high impedance) at different frequencies, thus behaving as switches controlled by the frequency of the sinusoidal signal through them. Nonetheless, the switches in the proposed architecture are needed after the rectifier where the complete sinusoid is lost and thus, the multiresonant circuits cannot work. Moreover, the piezo-crystals already act as frequency dependant impedances, as it is also shown by their lumped elements model in Chapter 2. A sinusoidal signal is generated and can reach the load only when the piezo is vibrating around its short-circuit resonance frequency. Other frequencies, different from higher harmonics, will only generate a negligible low signal not suitable for stimulation.

Therefore, the possibility of using MOSFET switches without a DC biasing for operating them was considered. This was reached in the proposed architecture by connecting two MOSFETs to the piezo-sources in such a way that they are powered and controlled by the input signal only. In particular, two circuit configurations are possible depending on the choice of a pMOS or a nMOS, as shown in *Figure 20*. V_{in} is the incoming sinusoidal signal and Z is the impedance of the load. The arrows represent the direction of the current through it. In (a) the bridge rectifier is allowing the passage of only positive pulses, when $V_{in} > 2V_d$, V_d being the voltage drop of a single diode. Moreover, M_1 is turned on for $V_{gs} < V_{th}$ (< 0), with V_g being the voltage at its gate, V_s the voltage at its source, and V_{th} the threshold voltage of the transistor. Therefore, the relation $V_{in} > 2V_d - V_{th}$ must be satisfied to let current pass through the load. Similarly, in (b), the bridge rectifier is allowing the passage of only negative pulses, and current flows through the load when $V_{in} > 2V_d + V_{th}$, with V_{th} being the positive threshold voltage of transistor M_2.

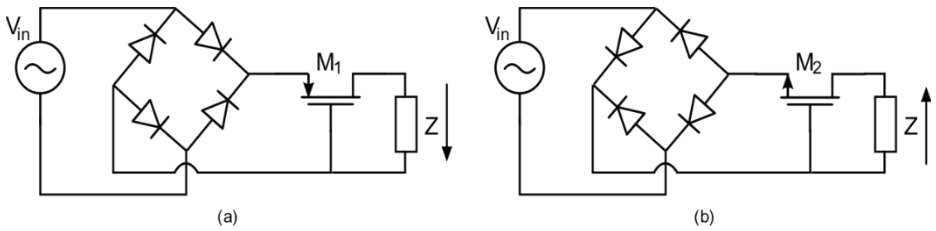

Figure 20. *(a) PMOS transistor M_1 used as a switch. (b) NMOS transistor M_2 used as a switch. The arrows represent the direction of the current through the load Z.*

In order to keep symmetry and reduce the choice of different components, p-channel MOSFETs were used as switches for both branches connected to the piezo transducers. The final circuit schematic can be seen in *Figure 21.* When P_1 is vibrating, the incoming signal is switching M_1 on, allowing current to flow from node C (i.e. cathode) to node A (i.e. anode), while M_2 turns off, thus avoiding current flowing through the diodes of the second bridge. Similarly, when P_2 is vibrating, M_2 turns on, while M_1 is off, and current flows from node A to node C.

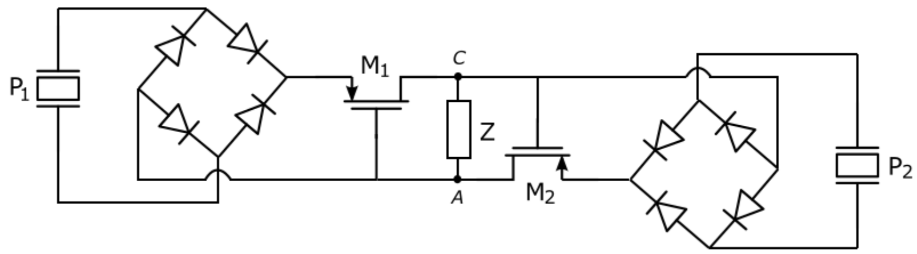

Figure 21. *Circuit schematic of final concept. Nodes A and C represent the anode and the cathode, respectively. Z is the impedance modelling the total electrodes-tissue interface.*

It can be noticed that power is not stored in the circuit since the switches operate only when ultrasounds are sent. Therefore, the control of the biphasic stimulation is taken out of the implant. The pulse width and the amplitude of each phase are adjusted by changing the duration and the intensity of the transmitted ultrasound bursts, respectively. Finally, the repetition rate of the biphasic pulses is controlled by the frequency of ultrasound transmission.

The operation of the final circuit was firstly simulated in LTSpice. Based on the results of simulations, suitable components were chosen to implement it on a Printed Circuit Board (PCB), and finally, the system was tested with piezoelectric transducers and electrodes, as explained in the next chapters.

4. Simulations

4.1. Definition of circuit schematic

LTSpice from Linear Technology was used as design simulation tool. For a first analysis, models of components that were already available in the simulator were selected (i.e. PMEG4010BEA Schottky diode and FDS4953 p-channel MOSFET), based on low voltage drop for the diodes and low V_{th}, low $R_{ds(on)}$ (on-resistance), and low Q_g (gate charge) for the pMOS. *Figure 22* shows the complete circuit schematic used in the simulator.

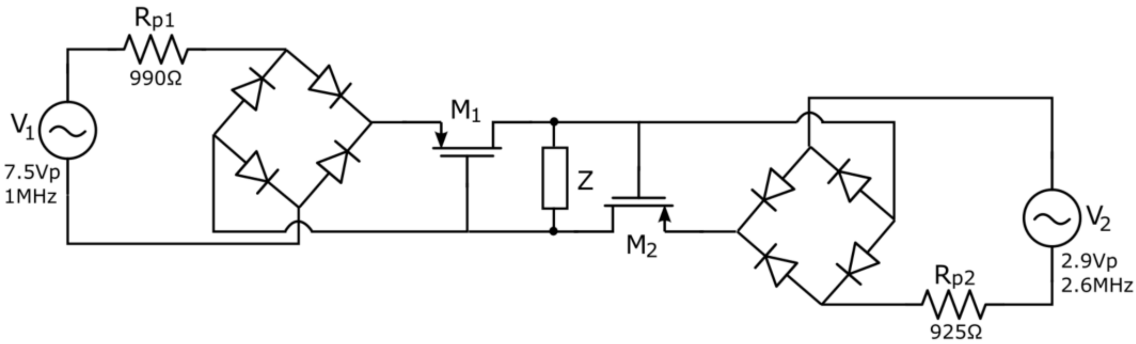

Figure 22. *Circuit schematic used for simulations in LTSpice.*

The maximum values of V_1 and V_2 were calculated considering a maximum η_{pc} and maximum I_{acou} in equation (11); these were found to be $V_{1,peak}$ = 7.5 V and $V_{2,peak}$ = 2.9 V. R_{p1} was calculated considering a PZT-5H piezo of thickness 1.05 mm, area 1 mm^2, resonant frequency 1 MHz, and air-backing (Z_{air} = 400 Rayls [69]); while, the resonant frequency of the second PZT-5H piezo is 2.6 MHz to avoid strong interference with the first piezo [56] and still harvest enough power with a thickness of 0.41 mm, and area of 0.16 mm^2. It must be noticed that for a specified load impedance (i.e. specific stimulating electrodes) and available input power P_{av}, the piezo transducers can be designed so that they show an optimal resistance R_p at resonance and the required voltage for stimulation is reached. In particular, R_p and the total input resistance of the circuit should be in the same range for maximum power transfer [44]. However, in the following simulations a fixed R_p is used to give a general overview of the circuit operation with a possible, although not ideal, transducer design.

Concerning the load Z, this can be modelled in two equivalent ways as shown in *Figure 23*. The voltage at node *Load* in (a) will be the same as the difference between the voltages at node *A* and

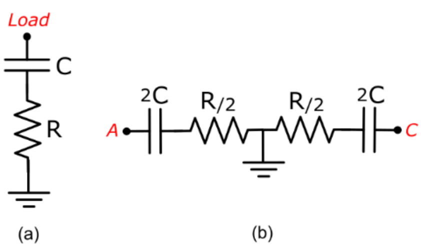

Figure 23. *Equivalent representation of circuit load: (a) is the equivalent series impedance of the two separated electrodes/tissue models in (b).*

node *C* in (b). The latter is closer to a real measurement setting, where reference to ground is not defined in the circuit, but from the external measuring probes.

Biphasic stimulation was simulated by alternatingly turning on the first and the second voltage source to obtain cathodic and anodic phase, respectively. Typical maximum pulse width (PW) for each phase is around 200 μs with an interphase delay (IPD) between 20 μs and 100 μs. Moreover, the pulse repetition rate (PRR) for standard peripheral nerve stimulation (PNS) or spinal cord stimulation (SCS) applications is 50-100 Hz, while higher PRRs (e.g. 500 Hz or more) are used for neuropathic pain treatment [87]. In the following simulations, a PW of 200 μs for both phases, IPD of 50 μs and PRR of 100 Hz are used, unless differently specified. The total injected charge at the end of each phase was obtained by plotting the integral of the current flowing through the load.

4.2. Results of simulations

4.2.1. General circuit operation and selection of components

Three main combinations of resistances and capacitances were used to model each electrode-tissue interface impedance: 200 Ω with 10 μF, 560 Ω with 1 μF (as used in [61]), and 2 kΩ with 100 nF. *Figure 24* shows the waveforms of the output voltage for each of these combinations considering a maximum transmitted power: the complete biphasic pulse includes the cathodic phase at 1 MHz and the anodic at 2.6 MHz, with a zoom of the high-frequency pulses.

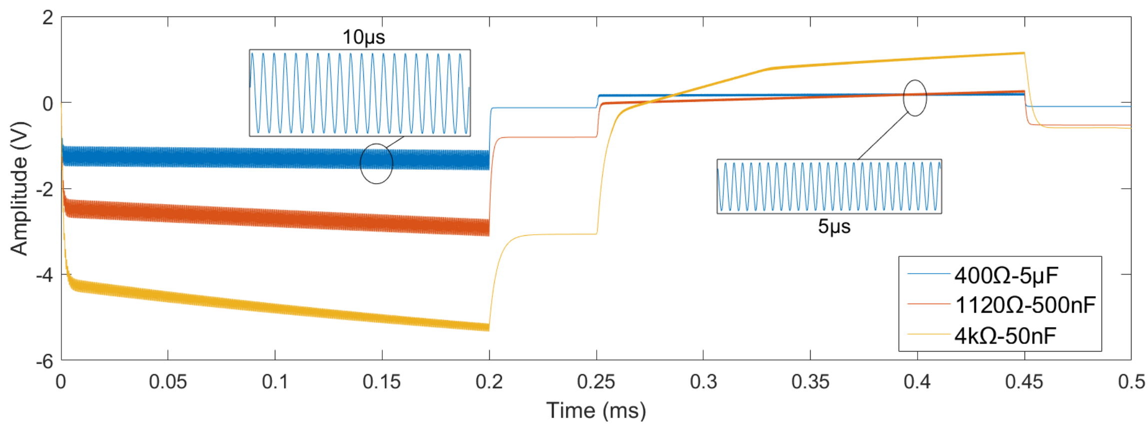

Figure 24. *Simulated output voltage waveforms for different load impedances with zoom of the high-frequency pulses for both phases.*

In the case of an ideal switch (i.e. short-circuit when turned on) and pure resistive load, the peak amplitude of the voltage at the load can be calculated with:

$$V_{load,peak} = \pm \frac{R_l}{R_l + R_p}(V_{oc} - 2V_d) \tag{13}$$

with a sign + for the anodic phase and – for the cathodic phase. V_{oc} is the amplitude of the input voltage source (i.e. the open-circuit voltage of the piezo transducer) and V_d = 0.2 V the voltage drop of each diode; R_l the total resistance of the load and R_p the transducer resistance. When introducing a capacitance C_l at the load, the peak voltage will increase in time from the value calculated in (13) with time constant $\tau = (R_p+R_l)C_l$. For instance, when considering the load with R_l = 1120 Ω, the initial peak voltage for the first phase should be around V_0 = -3.77 V. However, it can be noticed that $|V_0|$ is higher than the absolute peak value resulting from simulations and an offset is present in the output voltage. This is due to the presence of the MOSFET that does not charge and discharge fast enough within each UHF pulse. In fact, from *Figure 25* it can be seen that, with an ideal switch, the rectified signal reaches the right $|V_0|$ peak and the DC-offset starts from ~0.4 V (i.e. twice V_d).

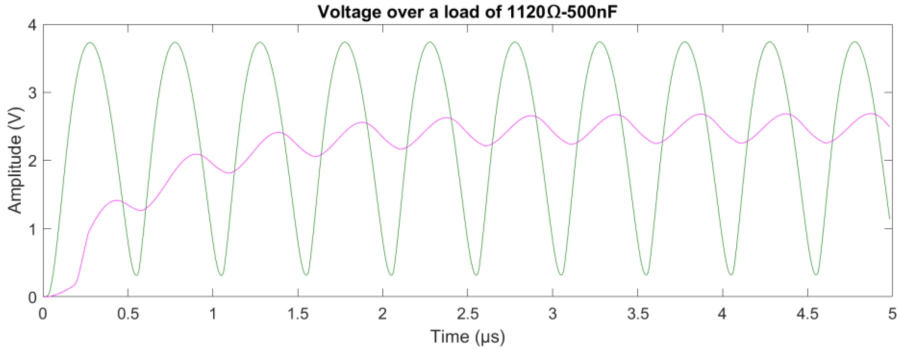

Figure 25. *Output rectified voltage at 1 MHz with an ideal switch (green) and with a pMOS between the bridge and the load (magenta).*

The offset of the output signal depends on the total gate capacitance of the MOSFET, which has to be charged and discharged at each cycle of the high-frequency input signal. The higher this capacitance, the slower is the switch, and thus, the higher the offset of the voltage at the output and the lower its peak amplitude. On the contrary, a low $R_{ds,on}$ of the pMOS gives a low voltage-drop across the device, and therefore, a higher signal peak amplitude at the output. The same observations are valid for the capacitance and the internal resistance of the diodes (see also Appendix B). Moreover, a low V_{th} for the p-channel MOSFETs is desirable for allowing operation at small input signal amplitudes.

New electrical components were chosen based on the previous observations. Therefore, diodes with voltage drop ≤ 0.2 V at 1 mA current and low junction capacitance were considered, and pMOS transistors were chosen with a trade-off between low V_{th} (i.e. greater than -1 V), low $R_{ds,on}$ (i.e. few hundreds of mΩ or less) and low gate capacitance/charge (i.e. less than 10 nC at V_{gs} = -5 V). The right selection of components was possible after some preliminary laboratory tests, as explained in Appendix B. Dual series diodes of Panasonic® DB3S308F put a in a bridge arrangement, and the NXP® p-channel trench MOSFET PMF170XP were finally selected. These components showed to give less offset, higher peak amplitude of the output voltage as well as lower leakage current than the components used in previous simulations.

As already explained, the presence of the switch is necessary to avoid the current from flowing to the opposite bridge and away from the load. However, a low leakage current could be observed in simulations flowing towards the non-working branch and gate of the MOSFET at each phase. This was shown to be dependent on the gate capacitance of the pMOS; the lower this capacitance, the lower the current through the gate. *Figure 26(a)* shows the simulated current through the load for a biphasic pulse using the model of the final components. *Figure 26(b)-(c)* illustrate the 1st and the 2nd phase, respectively. In these figures the red waveform is the current from the active branch (i.e. the pMOS drain current) of the specific phase, while the green waveform is the leakage current through the non-active branch.

4.2. Results of simulations

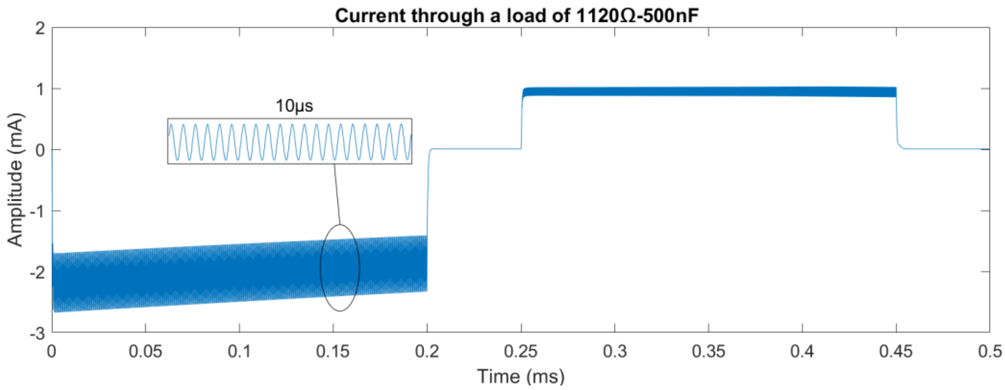

(a)

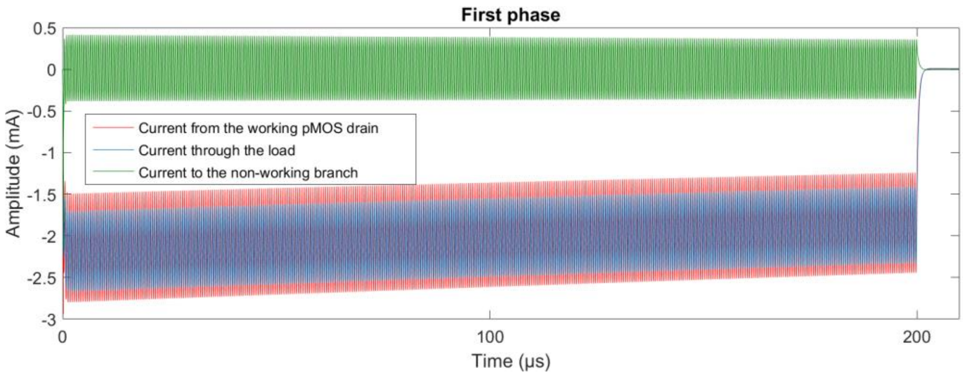

(b)

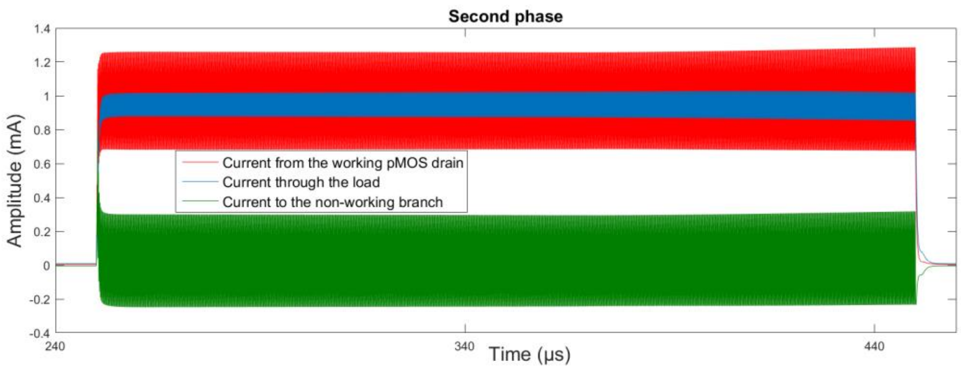

(c)

Figure 26. *(a) Simulated current through the load for a complete biphasic pulse. (b) Detail of the 1st phase with current through the working and non-working branch. (c) Detail of the 2nd phase with current through the working and non-working branch.*

4.2.2. Circuit limitations

The minimum input voltage for the correct operation of the circuit depends on the threshold voltage of the transistor, which has a typical value of -0.9 V from datasheet, and it is confirmed by DC sweep analysis as shown in *Figure 27*. The LTSpice model of the selected p-channel MOSFET (i.e. PMF170XP) shows generally a low on-resistance for all the input voltages with a maximum of 13 kΩ for an input close to 0. Around 0.6 V there is a turning point, at which the drain current starts increasing more linearly with the input voltage. Rds also decreases rapidly reaching low values of tens of Ohms after a V_{sg} input of ~0.8 V. These results suggest that the piezo-source should provide an input voltage that assures a V_{sg} of at least 0.6 V. This will be affected by the voltage drop of the diodes and the impedance of both the load and the transducer. Concerning the maximum input voltage, this depends on the maximum voltage ratings of the transistor, which is V_{gs} = ±12 V for the chosen MOSFET.

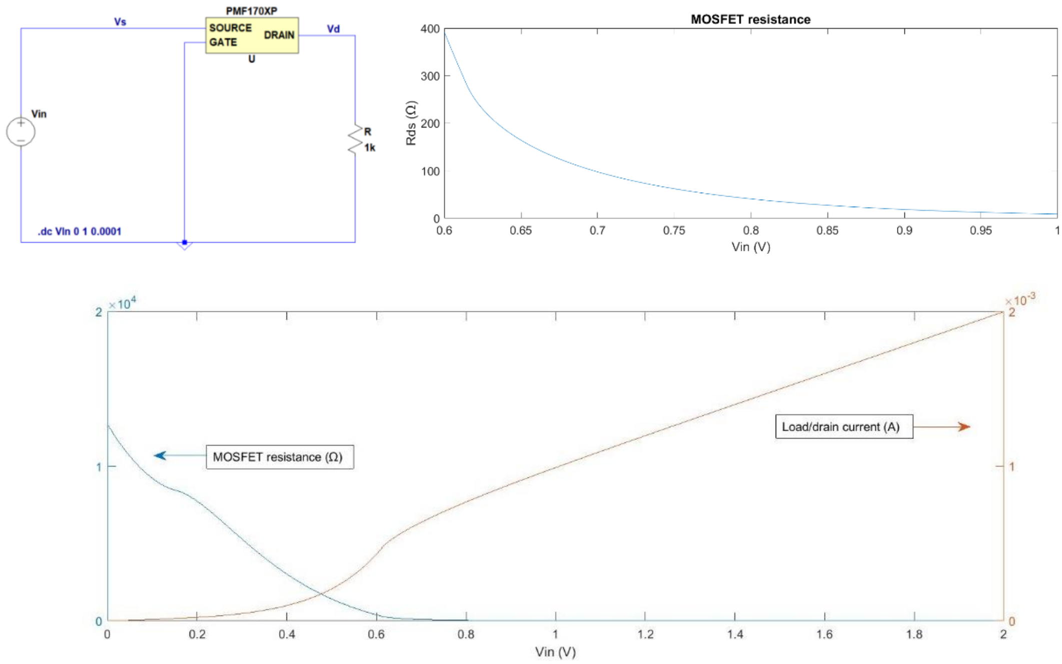

Figure 27. *DC sweep analysis circuit (top left), result of the analysis (bottom), and detail of the MOSFET resistance curve (top right).*

4.2.3. CHARGE BALANCING

For the purpose of charge balancing, the charge injected in the cathodic phase should be completely reversed in the anodic phase. Because of the different frequencies and amplitudes of the two piezo-sources, the charge injected in one phase differs from the other for the same PW. This is seen in *Figure 28* for different loads: the value of the charge stored in the load after each phase is indicated. The 2nd piezo generates a lower signal than the 1st one and thus, the anodic current is too low to bring the charge value to zero. This results in charge accumulating at the electrodes-tissue interface with a consequent offset voltage until the next biphasic pulse as shown in *Figure 29*. This offset is acceptable as long as it does not exceed the water window for the specific electrodes/tissue interface, as discussed in chapter 2.

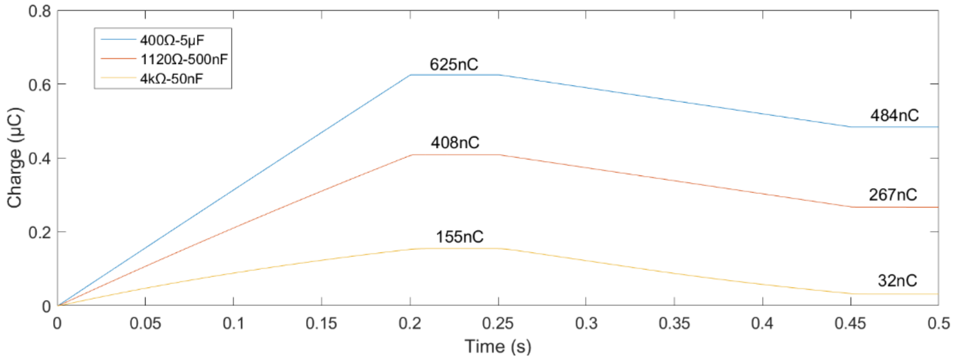

Figure 28. *Charge delivered to the load for three different load impedances and maximum input.*

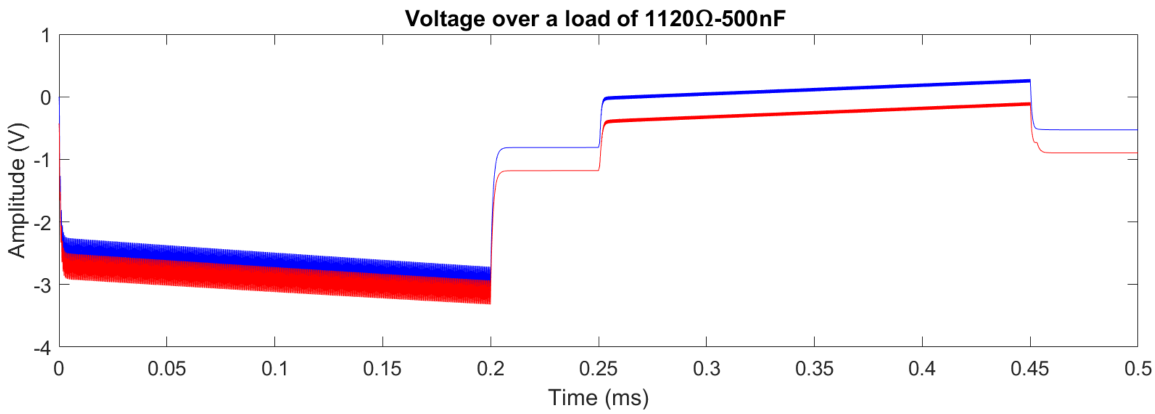

Figure 29. *Comparison of two biphasic pulses with a delay of 9.55 ms between the end of the first one (blue) and the onset of the second one (red).*

If, for example, we want to inject 0.2 µC in one phase and then reverse it, the PW must be changed as in *Figure 30*. For small load impedances the PW is reduced for both phases; however, in the case of a large impedance (i.e. small electrodes) the PW is increased over 200 µs to reach injection of 0.2 µC. For even smaller electrodes, and thus higher impedances, only less charge can be injected in the same period. For instance, when simulating a load of 12 kΩ and 5 nF (i.e. the series of two electrodes of 6 kΩ and 10 nF each) with a 7.1 V input (i.e. V_{oc}-$2V_d$), the maximum charge that can be injected is of 5 nF x 7.1 V = 35.5 nC. This must be taken into account especially when considering higher levels of charge that might be needed for human nerve fibres activation [88]. Finally, the shown waveforms were obtained by monitoring the charge over time and stopping the cathodic and the anodic phase when 0.2 µC and 0 C were reached, respectively. Nonetheless, the designed circuit lacks a charge monitoring function. As already discussed in Chapter 3, this should be included for proper charge balancing.

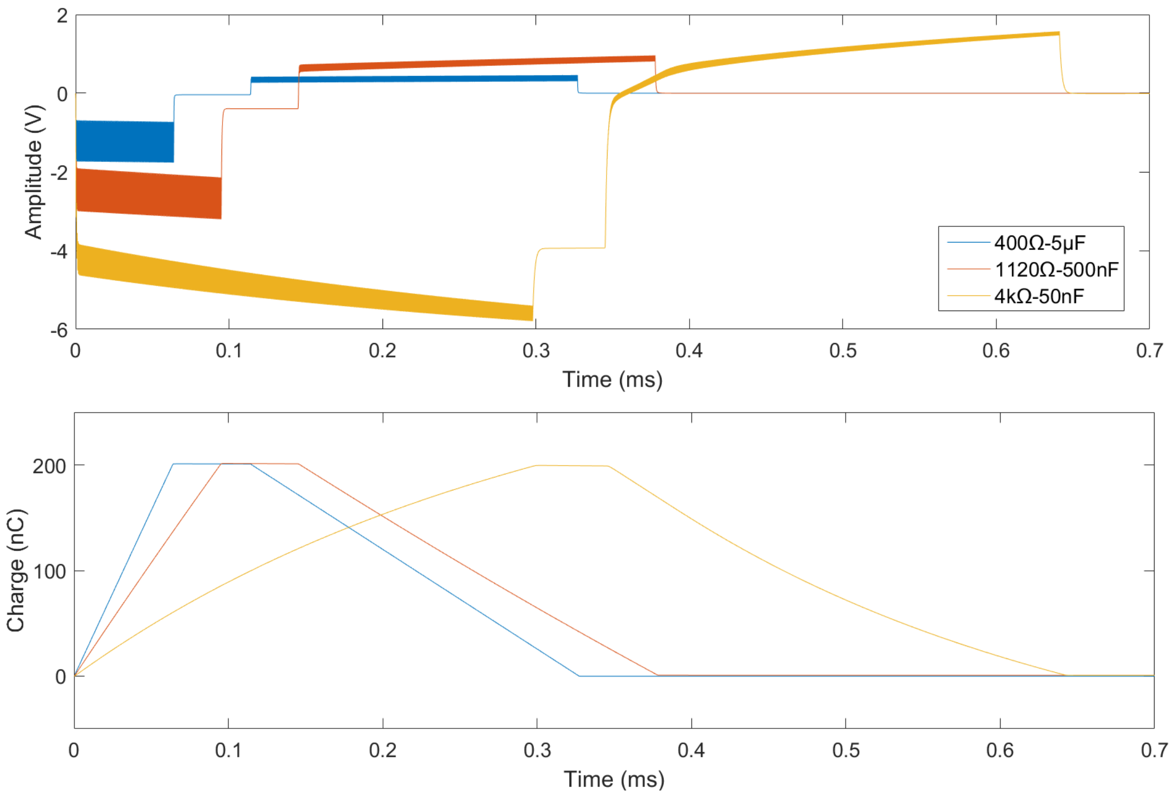

Figure 30. *Simulated voltage at the load (top) and injected charge (bottom) for three different load impedances using models of the final components.*

4.2.4. POWER EFFICIENCY

The model of the piezo-impedance was completed with the addition of the RLC branch and the electrodes capacitance C_0 as in *Figure 12(a)* of Chapter 2 and compared with the simplified purely resistive model. The current through a 1 kΩ load with a PW of 100 µs is plotted in *Figure 31* for both cases. It can be observed that, when using the complete resonance model, the shape of the waveform slightly changes; however, there is not a significant impact on the signal amplitude.

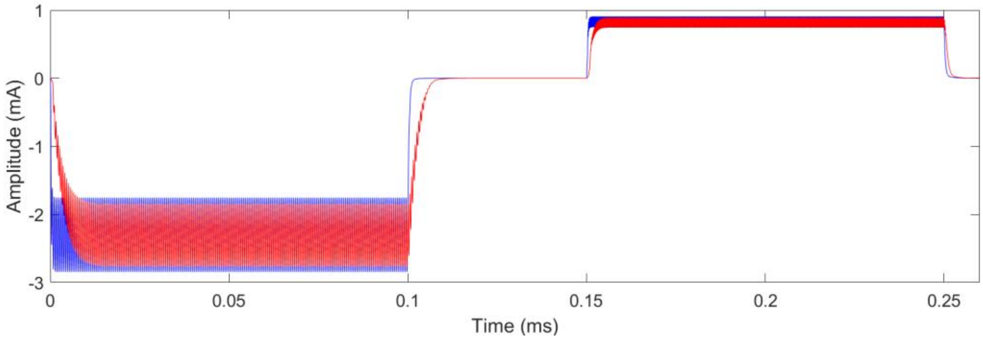

Figure 31. *Current through a 1 kΩ load with the purely resistive piezo-impedance model (blue) and the complete resonance model (red).*

An input signal at 1 MHz was used when calculating the efficiency of the circuit; this was defined as the ratio between the power at load (P_{load}) and the power at the input of the rectifier (P_{in}), which in a real setting will depend on the transmitted acoustic intensity, as defined in equation (11). P_{load} and P_{in} were calculated as shown in *Figure 32*.

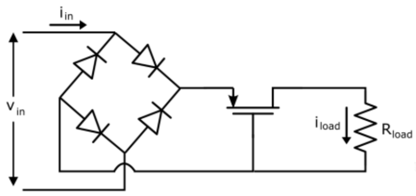

$$P_{in} = V_{in,rms} \times I_{in,rms}$$
$$P_{load} = I_{load,avg}^2 \times R_{load}$$

Figure 32. *Calculation of power efficiency for the illustrated circuit. The subscripts rms and avg refer to the root-mean-square and the average value of the signal, respectively.*

P_{load}/P_{in} was found for different load impedances and it is reported in *Figure 33* for increasing P_{in} values. The efficiency drops for lower loads since, for the same input power, the output signal decreases with lower load impedances.

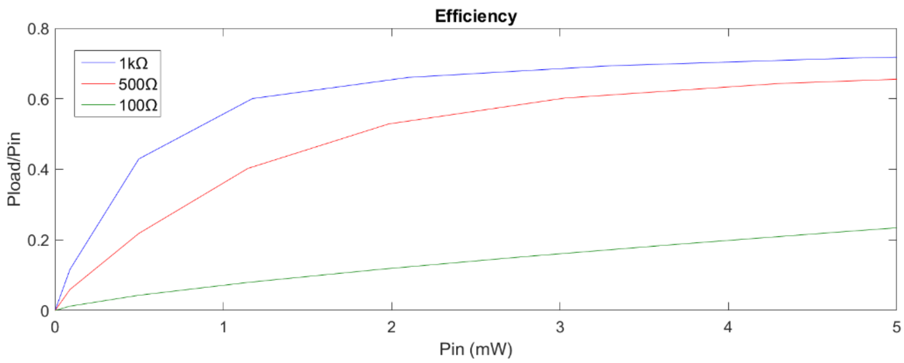

Figure 33*. Simulated power efficiency of the designed circuit for different load impedances.*

4.2.5. INTERFERENCE FROM HIGHER HARMONICS

The interference from higher harmonics was simulated by adding an extra RLC branch to the 1 MHz transducer impedance in order to model its 3 MHz harmonic (*Figure 34(a)*). Therefore, the two voltage sources in the Spice schematic of *Figure 22* were switched on simultaneously during the 2nd phase. The resulting waveform is shown in *Figure 34(b)* in red for 1 kΩ load and PW of 100 µs. During the 1st phase only the 1 MHz source is working with V_{oc1} = 7.5 V. To model the interference of a 2.6 MHz transmitted wave over the first piezo, both sources are made work at 2.6 MHz in the 2nd phase with V_{oc1} = 2 V and V_{oc2} = 2.9 V. V_{oc1} was calculated considering the first piezo being in the -6 db beam of the 2.6 MHz wave. It can be noticed that the signal from the first source gives interference in the 2nd phase, resulting in lower current amplitude compared to the scenario without interference (blue waveform).

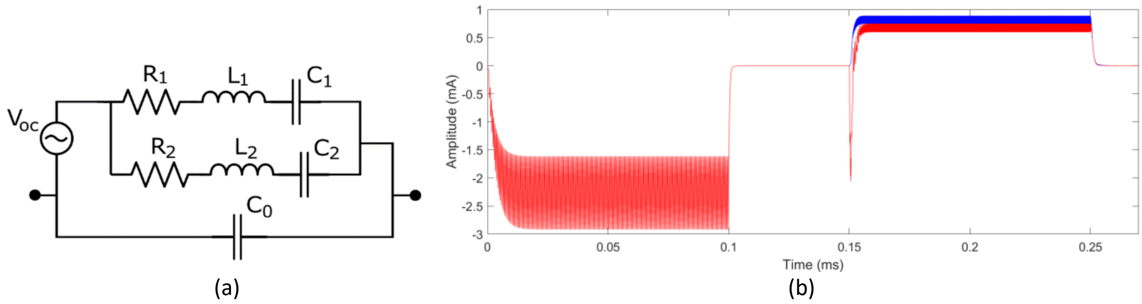

Figure 34. *(a) Model of piezo-impedance with extra RLC branch for higher harmonic. (b) Simulated current through 1 kΩ load with (red) and without (blue) interference of the 1 MHz piezo on the 2nd phase.*

In a real setting, interference would occur if the transmitters are not aligned correctly with the respective receivers and their beams reach both receivers instead of one. This could be avoided by putting the receivers aligned with the corresponding transmitters. In particular, the 1 MHz receiver should be put outside of the ultrasonic beam of the 2.6 MHz transmitter, and vice versa. Other solutions include the use of focused transmitters, narrow-bandwidth receivers or the use of a second receiver that has a higher resonant frequency (>3 MHz). However, this would require the design of an even smaller transducer, which should still harvest enough power to switch on the pMOS and to stimulate.

5. Measurements

5.1. Measurement setup

Simulations ran in LTSpice helped in the correct selection of the components to be included in a fabricated prototype of the system. Moreover, some limitations of the topology were highlighted and the results suggested what to expect from the output signal in terms of amplitude range and waveform shape. Nonetheless, measurements were conducted with a PCB and available piezoelectric transducers to verify the correct operation of the proposed architecture with real components.

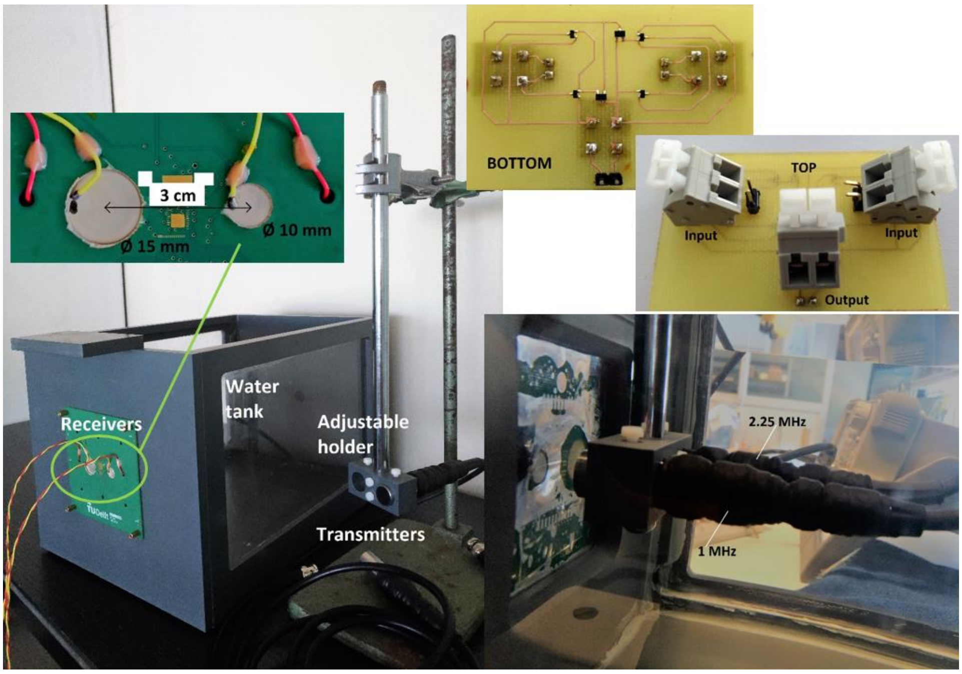

Figure 35. *On the left, setup with transducers and water tank. On the top-right, pictures of the top and bottom sides of the fabricated PCB. On the bottom-right, picture of the transmitters in water aligned at about 3 cm-distance with the receivers on the other side of an acoustic transparent membrane.*

5.1.1. Electronics and electrodes

A PCB (*Figure 35, top-right*) was designed and fabricated in the TUDelft bioelectronics group. The circuit was then interfaced with different loads (i.e. resistors and capacitors) via a breadboard. PtIr electrodes were also used as a load in the final measurements. Their impedance was measured with the results shown in Appendix C. Monopolar measurements gave a mean value of around 4204 Ω at 1 kHz.

5.1.2. Piezoelectric transducers

The design of optimal piezo-elements was not in the scope of the project. Therefore, piezoelectric transducers provided by the TUDelft Imaging Physics group were used; these did not match the characteristics of the elements used in simulations. However, they were suitable for showing the operation of the circuit with the transmission of ultrasonic waves in water.

The transmitters were Olympus® unfocused immersion transducer with a nominal element size of 13 mm and resonance frequencies of 1 MHz and 2.25 MHz. The transducers already include a front wear plate, which acts as a matching layer for water, and a backing to attenuate reflection of the signal from the back of the active element [65]. The cable that transports the signal to/from the transducer is a standard coaxial cable with a male-BNC connector at the distal end that can be connected to a waveform generator. Finally, this kind of transducers could not be used as receivers because of the presence of the heavily-damping backing, as explained in Appendix B.

The receivers were two PZT disc-shaped elements mounted on a rectangular board for interfacing with the water tank while keeping air-backing, as in *Figure 35*. The smaller element (P1) is 2 mm thick and has an impedance of around 200 Ω at 1 MHz. Whereas, the larger element (P2) has a thickness of 0.5 mm and impedance of 12 Ω at 2.25 MHz. Their complete impedance magnitude and phase was measured for different frequencies as in *Figure 36*. The receivers were then connected to the circuits via two wires soldered to the front and back electrodes. Finally, they were coupled to water thanks to transmission gel and the contact with an acoustic transparent membrane.

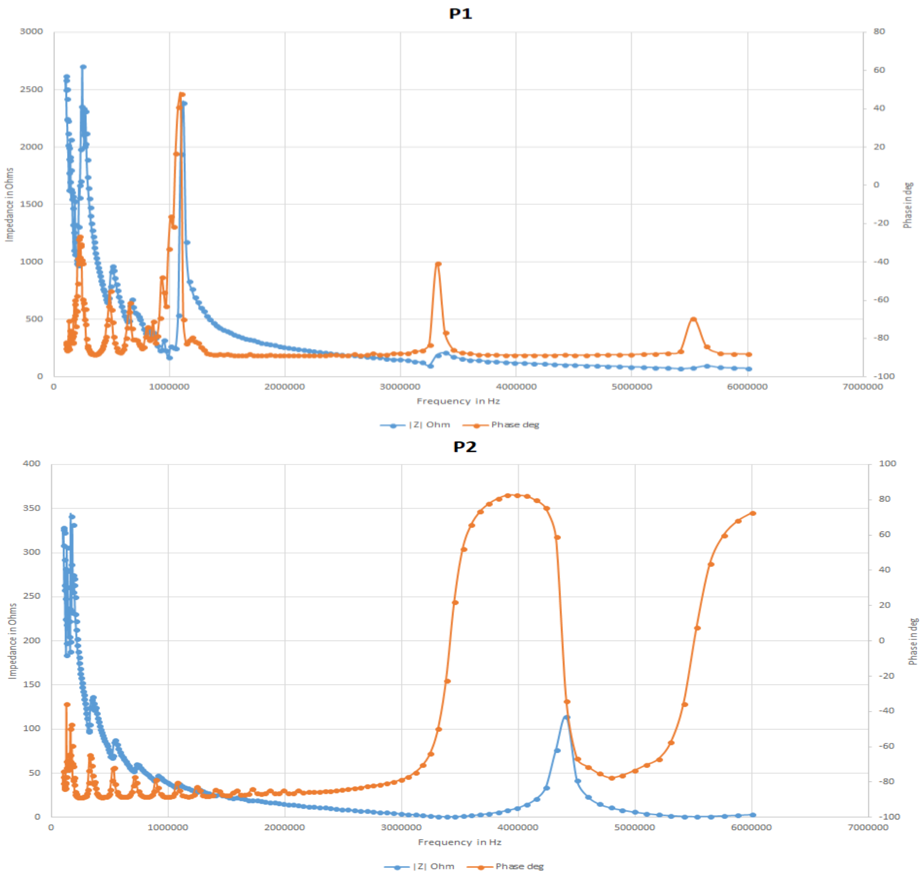

Figure 36. *Impedance magnitude and phase for the two piezoelectric receivers P1 and P2.*

5.1.3. Extra equipment

An arbitrary waveform generator was used to drive the transceivers. The duration and repetition rate of the tone bursts could be programmed, along with the amplitude and frequency of the exciting waves. Moreover, a delay could be set between the 1 MHz and the 2.25 MHz signals. In this way, the parameters of the biphasic stimulation could be selected by changing the settings of the waveform generator. Furthermore, two power amplifiers were used to amplify the signal from the waveform generator before using it to activate the transmitters. Finally, an oscilloscope was utilised to visualize the voltage at different terminals of the circuit.

5.2. Results of measurements

5.2.1. Monophasic stimulation

For the following measurements only the 1 MHz transmitter at about 3 cm distance was used. The excitation voltage was 42 Vpp for 50 cycles and 10 Hz PPR. *Figure 37* shows the received open-circuit voltage and the output voltage for three different load impedances with zoom of the high-frequency pulses. The difference in the amplitude for changing load is in line with simulations: a small impedance (yellow waveform) gives a lower amplitude and smaller offset than higher impedances. Moreover, when two impedances of 560 Ω and 1 µF are put in series at the load, an offset is observed before and after the monophasic pulse due to the charging of the capacitors.

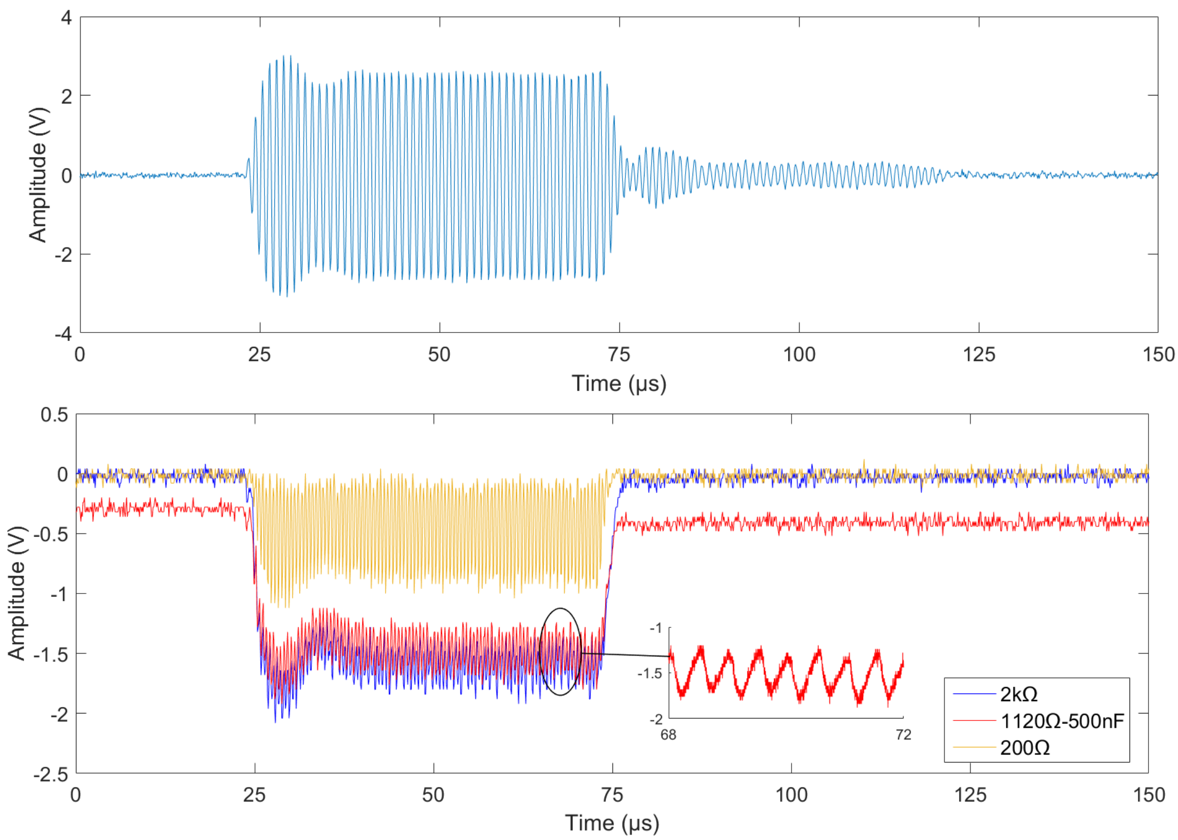

Figure 37. *Top: received open-circuit voltage at 1 MHz. Bottom: output voltage for three different load impedances and detail of the high-frequency pulses.*

When driving a pair of PtIr electrodes in PBS, the excitation voltage at the transmitter was 56 Vpp. A monophasic pulse of 100 µs with PPR of 100 Hz was used. *Figure 38* shows the open-circuit voltage at the receiver and the voltage across the electrodes. The capacitive nature of the electrodes-electrolyte interface is observable from the increase of the signal baseline.

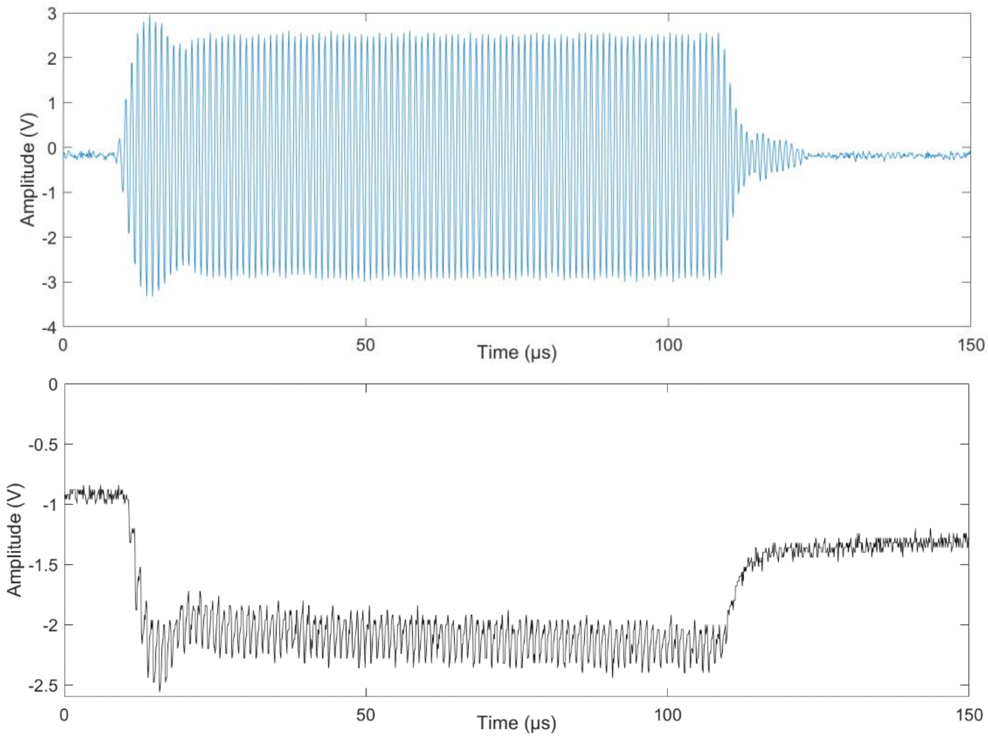

Figure 38. *Voltage across PtIr electrodes in PBS (bottom) as a result of a 100 µs – 100 Hz monophasic stimulation obtained from a received 1 MHz signal (top).*

5.2.2. BIPHASIC STIMULATION

For the following measurements the transmitters were put between 2 and 3 cm distance from the receivers. The excitation voltage was 56 Vpp for 200 µs for the 1 MHz transceiver, and 190 Vpp for 100 µs for the 2.25 MHz transceiver. *Figure 39* shows the open-circuit voltage at the two receivers: the 1 MHz signal is the input for the cathodic phase, while the 2.25 MHz one is the input during the anodic phase of the biphasic pulse. The IPD was set to 50 µs.

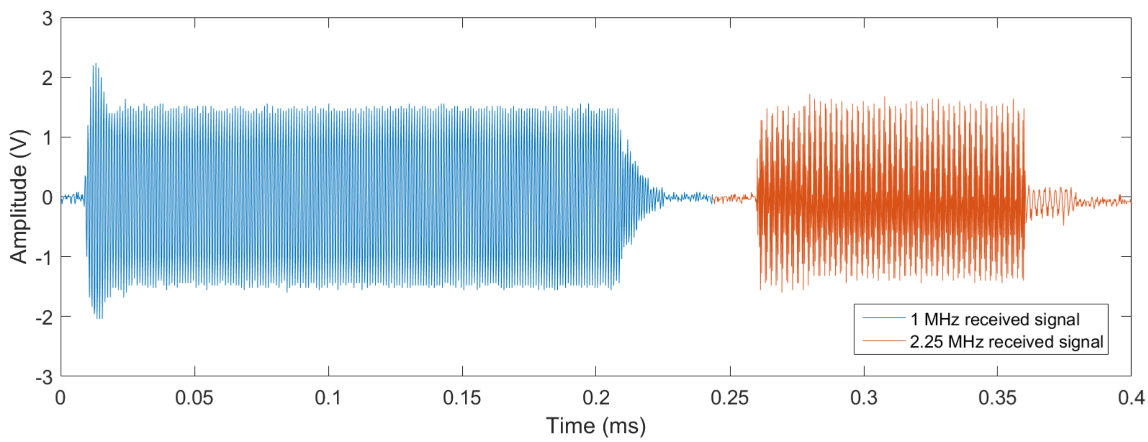

Figure 39*. Open-circuit voltage measured at the two receivers.*

Firstly, a resistive load was connected to the output of the circuit and the voltage across it was measured. This is seen in *Figure 40* with a zoom of 5 µs of the UHF-pulses during the 1st and the 2nd phase.

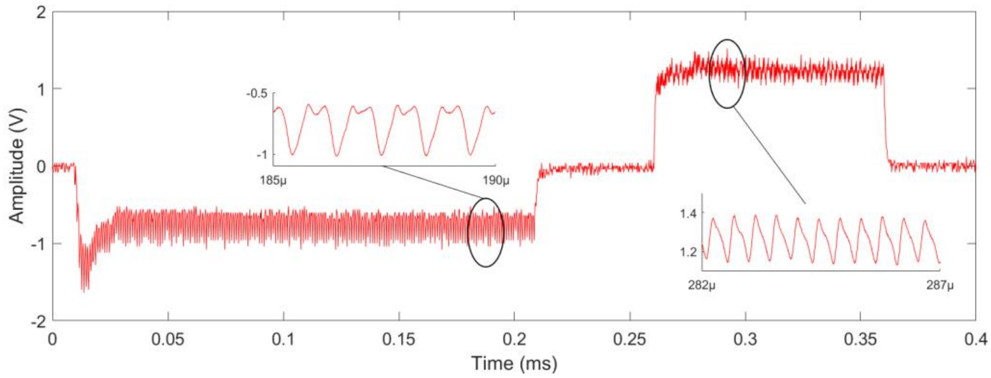

Figure 40*. Biphasic signal across a 2 kΩ load with detail of the UHF pulses of both phases.*

It can be noticed that the pulses of the cathodic phase are different in amplitude at each cycle. Concerning the anodic phase, 11 pulses are found in 5 µs. However, for a 2.25 MHz rectified wave, 22.5 pulses should be observed in 5 µs. This is due to the different amplitudes of the signal received by the front and back electrode plates of each receiver. These signals are plotted in *Figure 41* for the 1 MHz receiver and the 2.25 MHz one. The former gives a higher signal from the front electrode (i.e. the one interfacing water), while the latter has a higher signal from the back electrode (i.e. the one exposed to air) and almost zero-signal from the front.

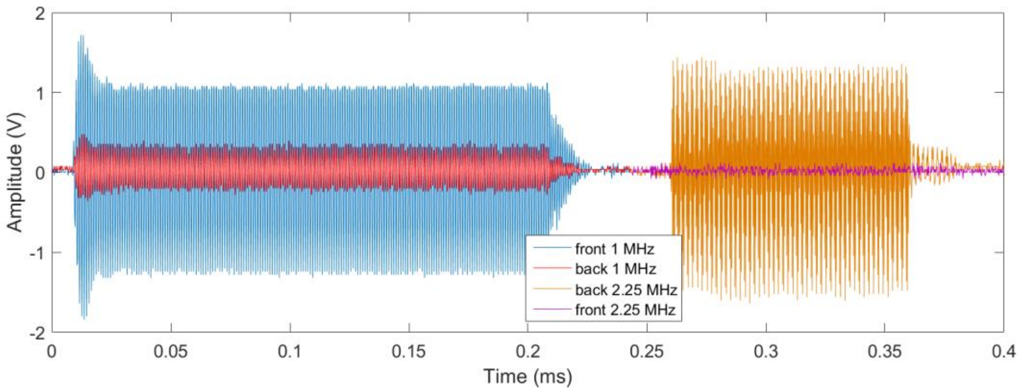

Figure 41. *Signals from front electrode plate and back electrode plate for both receivers.*

Biphasic stimulation was also tested with PtIr electrodes. The voltage at the output is plotted in *Figure 42.* After the anodic phase the voltage across the load does not drop instantly to zero due to the capacitive nature of the electrodes inside the solution. This suggests that the anodic phase should be longer to completely reverse the charge injected in the cathodic phase. Alternatively, for the same PW, the amplitude of the 2nd phase should be higher.

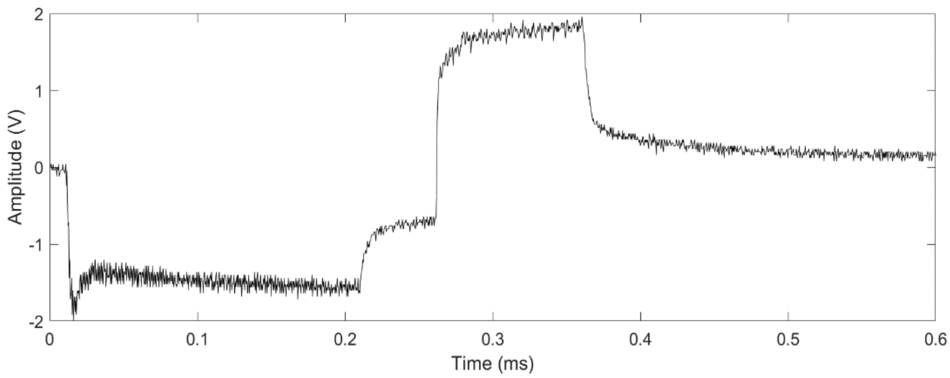

Figure 42*. Voltage recorded across a pair of PtIr electrodes for a biphasic input.*

The current through the load was obtained by measuring the voltage across one 1 kΩ resistor in series with the electrodes as in *Figure 43.* As the voltage increases, charging the capacitance of the load, the current exponentially decreases.

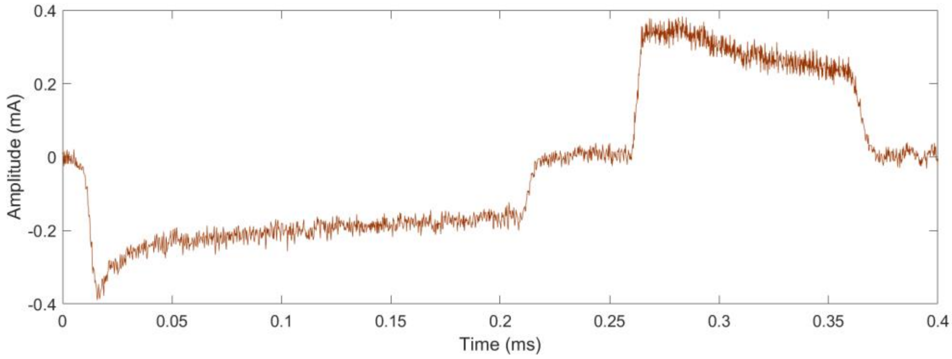

Figure 43. *Current recorded between two PtIr electrodes for a biphasic input.*

Finally, for all the presented biphasic pulses a PRR of 10 Hz was used. However, this could be changed by adjusting the period of the transmitted ultrasonic burst, and a 100 Hz biphasic stimulation could be recorded as in *Figure 44*.

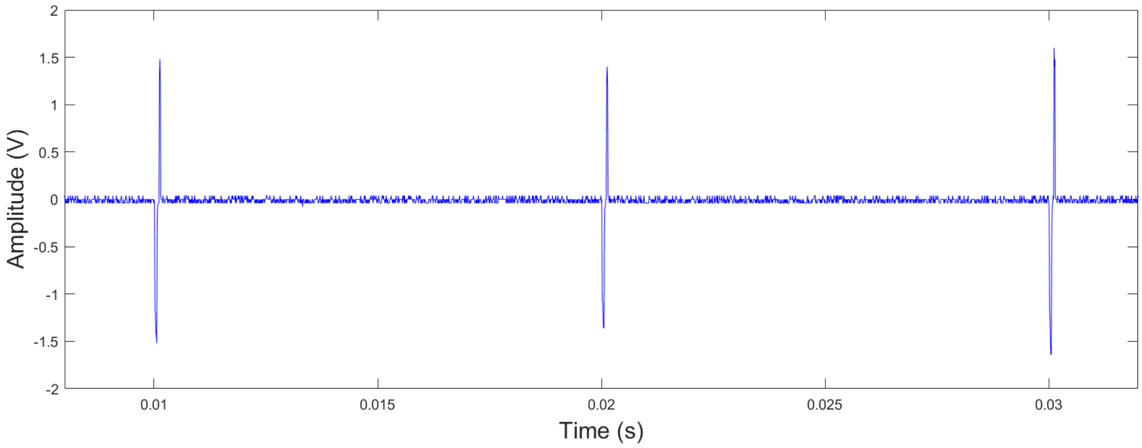

Figure 44. *Biphasic pulses at the load for a 100 Hz repetition rate.*

5.2.3. EFFICIENCY

Efficiency of the circuit was calculated by measuring the input (i.e. rectifier input) and the output (i.e. at the load) power having an ideal sinusoid changing in amplitude as source. The result is plotted for two frequencies in *Figure 45.* The efficiency of the circuit becomes lower for higher frequencies. For both frequencies, the measured efficiency with low load (i.e. 100 Ω) is smaller than the one calculated with higher loads for all P_{in}. This result was also found in simulations as shown in Chapter 4.

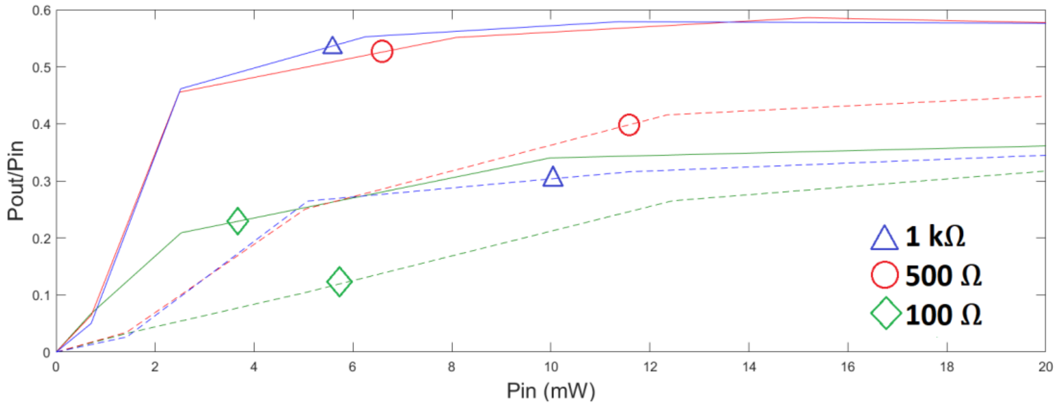

Figure 45. *Power efficiency calculated for three different loads and two input frequencies. Solid lines are for a 1 MHz input, while the dashed lines are for a 2.6 MHz one.*

5.3. Discussion

The results of measurements showed the ability of the designed circuit to operate with an input voltage obtained from real piezoelectric transducers. The PW, IPD, PRR and amplitude could be controlled by changing the parameters of the waveform generator driving the transmitters. Moreover, the system was capable of driving a pair of PtIr electrodes in PBS.

The change of the output voltage depending on the load was in line with simulations. The output waveform followed the variations of the input signal. Nonetheless, the vibrations of the piezo after the end of the stimulating pulse do not appear at the output since the fading signal is too low for switching on the bridge and the pMOS.

The difference in signal amplitude between the front and back electrode of the same transducer gave a different amplitude between individual UHF pulses, especially for input voltages lower than 4 Vpp. This difference might be the consequence of inhomogeneities in the transducers used, and thus in a charge distribution inside the material that gives higher signal on one electrode than on the other when not biased. This should be further analysed having more information about the material and its polarization and should be taken into account in a future design of the transducers.

The alignment of the transmitters and receivers was adjusted manually. It was noticed that by changing the angle and distance between them, the received signal was decreasing in intensity and the effect of the reflected waves was more evident (see Appendix D). Therefore, when the device is implanted, particular care should be taken of how to obtain good alignment between the external transducers and the millimetre-sized receivers inside the body.

High voltages were used to drive the transducers in order to reach at least 2 Vpp at the receivers. The poor transmission efficiency could be in part explained by the lack of a matching layer between the receivers and water, and, for the bigger piezo-receiver, by the operation at a frequency (2.25 MHz) different from the resonant one (around 4 MHz). More suitable transducers for both transmission and reception of the signal should be designed in order to effectively stimulate while keeping a safe value of the transmitted acoustic intensity and pressure.

The efficiency of the circuit (i.e. bridge rectifier and pMOS) is affected by the frequency and impedance of the source and the impedance of the load. It was observed that higher frequencies give lower efficiency. Moreover, the simulated efficiency was higher (*Figure 33*). This is due both to the different signal presented at the input of the rectifier between simulations and measurements and to the Spice model of the pMOS, which gives better performance in simulations than in real measurements, especially for high frequencies (see also Appendix B).

Concerning the transmission efficiency, this is defined as the ratio between the available electrical power at the receiver (P_{av}) and the power at the input of the transmitter. This was not calculated as the transducers used in measurements could not be characterized and were not optimized for power transfer. Despite so, the link efficiency should be analysed in a complete system. This will depend on different aspects:

- η_{pc} of both the transmitter and the receiver.
- Distance between the transducers. The sound pressure has a loss of 0.0022 dB/cm in water and of 0.54 dB/cm in soft tissue at 1 MHz [69].
- Alignment between the transducers. The axial and transverse angles of the receiver with respect to the transmitter affects P_{av} at the receiver [89].
- Acoustic coupling between the transducers and the propagation medium. In particular, an application-specific matching layer has to be designed to avoid reflections.

Finally, electrical impedance matching is necessary for having maximum power transfer between the receiver and the loading circuit. A mismatch between the electrical impedance of the receiver and the impedance of the circuit leads to a decreased overall power efficiency.

6. Conclusion

We proposed a neural stimulator performing UHF biphasic neural stimulation by harvesting ultrasound waves. Two different piezoelectric receivers were chosen to reverse the current through the tissue and thus obtain biphasic pulses without the need of extra power supply and internal control for the switches. Similar stimulators, which also do not require power storage, using IC [78] or ultrasounds [40] are only capable of monophasic stimulation and half-wave rectification of the received signal, as opposed to our design. The former aspect could lead to damage of the electrodes and/or tissue, while the latter wastes half of the energy of the input sinusoid. Moreover, state-of-the-art biphasic neural stimulators powered by ultrasounds [81], [82] use constant current pulses as stimulation technique, thus requiring the DC-conversion and regulation of the AC input signal. Contrary, the proposed system does not necessitate the conversion to a DC regulated voltage for obtaining constant pulses, and does not store power for supplying the electronics as in the UHF stimulator reported in [61]. These fundamental differences allow for a simple architecture with few components in which the power consumption only depends on one bridge rectifier and one MOSFET at each phase, thus giving high-power efficiency. Furthermore, the control of the stimulation parameters (i.e. amplitude, pulse width, interphase-delay, frequency) is performed externally by adjusting the parameters of the transmitted ultrasonic signal.

A prototype was tested with commercial transducers resulting in biphasic pulses between a pair of stimulating electrodes. Nonetheless, once a suitable pair of piezoelectric receivers will have been designed to be integrated with the proposed circuit, the complete system could be implanted and tested *in vivo* to verify the efficacy of stimulation. Considering the dimensions of the selected components and a maximum of 1 mm^2 area for each piezo, the total surface area of the device could go down to approximately 30 mm^2. Finally, the device does not provide multiple stimulation channels and real-time charge injection control. However, the advantage of such a design will be the possibility of investigating the effect of UHF biphasic stimulation in recruiting small peripheral nerves with a complete external control of stimulation.

7. Future work

Future work for the presented system includes:

- Selection of better performing electrical components, such as high-speed MOSFET switches and ultra-low drop diodes, for higher power efficiency.
- Design and fabrication of piezoelectric transducers to be integrated with the circuitry in a complete implantable device. This will require:
  - investigation of different transducers materials (e.g. various ceramics, and polymers, as PVDF), dimensions and geometries to obtain the most efficient ultrasonic link. The selection of optimal transducers will especially depend on the selected frequency for stimulation, the depth of the implant and the impedance of the load that has to be driven;
  - selection of biocompatible materials for protection of the system and interface with the tissue (e.g. polyimide, epoxy, silicon rubber, etc…);
  - consideration of implant mechanical properties based on the implantation site.
- Finite element modelling of the complete implantable device in order to analyse the impedance of the designed transducers and have an estimation of the power that can be harvested.
- Design of an ultrasound transmitter array for optimal alignment with the implanted receivers and high power-conversion efficiency.
- Experiments in small animals to assess the efficacy of stimulation.
- Control over injected charge and inclusion of a charge balancing technique; ideally, power storage and regulation functions are not added. Alternatively, different piezo-elements could be used for driving the different parts of the stimulator: one for direct UHF stimulation, and the other for power supply.
- Design of data communication module for scaling up the number of stimulation channels, controlling the various functions of the stimulator and for closed-loop operation of the system. Data can be received while powering the implant, or hybrid systems (IC communication and US powering) could be investigated.

APPENDICES

A. Lumped elements models for piezoelectric transducers

Krimholtz, Leedom, and Matthae (KLM)

The KLM model for a piezoelectric transducer represents the system comprising the piezo element with electrodes on the top and the bottom face, and the front and back acoustical media with a three-ports network, as shown in *Figure 46(a)*.

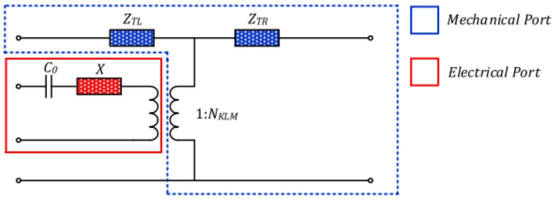

(a)

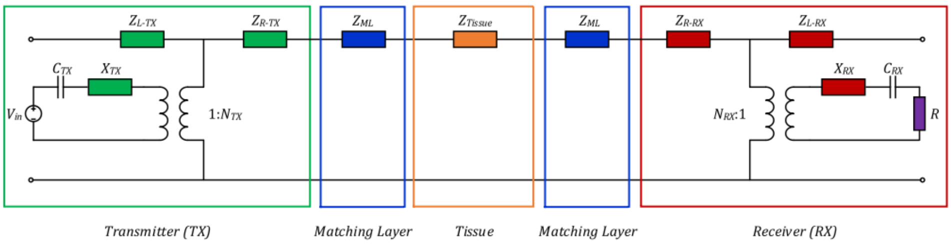

(b)

Figure 46. *KLM model for (a) a piezoelectric transducer, and (b) an acoustic power transfer system [26].*

C_0 is the plate capacitance from the electrodes, and X is the frequency dependent acoustic capacitance, which is zero when operating the transducer at resonant frequency. The thickness of the transducer is half the wavelength of the ultrasounds in the material. N_{KLM} is frequency-dependent turn ratio of the transformer. Finally, Z_{TL} and Z_{TR} represent the impedance of the backing medium and the front acoustical load of the transducer, respectively.

Figure 46(b) shows the KLM equivalent model for a complete acoustic power transfer system where also the impedance of the tissue and of the matching layers for both transmitter and receiver are considered.

Model for Spice simulator

Deventer et al. [74] illustrated a PSpice one-dimensional model for an ultrasonic transducer. The authors based their work on the approach of Püttmer et al. [73] with the assumption of plane longitudinal waves. The schematic of the circuit is reproduced in *Figure 47* for LTSpice simulator.

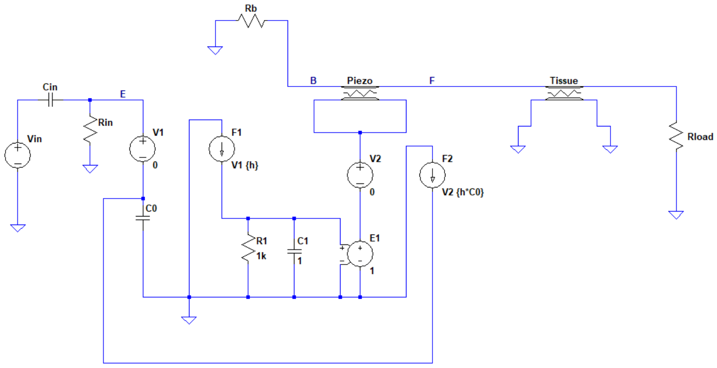

Figure 47. *LTSpice schematic of a piezotransducer model reproduced from* [74].

The piezoelectric transduction is modelled with current-controlled current sources F1 and F2, and the parts involving acoustic waves propagation are modelled with lossy transmission lines -Piezo and Tissue in the figure-. When an input pulse is applied at node E (i.e. electrical port), the current through the capacitor C0 controls F1 with gain h. Its output is then integrated by C1 giving the total charge that deforms the transducer. The electrical currents at nodes B and F (i.e. acoustical ports) give the rate of deformation; their difference controls F2 with gain h*C0, resulting in a voltage across C0 that is proportional to the transducer deformation. In the thickness mode, the constant h (N/C) can be found with:

$$h = \frac{e_{33}}{\varepsilon^S} \tag{14}$$

e_{33} being the piezoelectric stress constant (C/m^2), and ε^S the permittivity with zero or constant strain.

This model was shown to be useful when determining the speed of sound and the attenuation of ultrasounds in a pulse-echo setup.

B. Preliminary circuit tests

The first selection of circuit components went for the Bourns® Schottky diodes bridge rectifier CD-HD2004, and for the Diodes Inc® p-channel enhancement mode MOSFET DMP3098LQ. All the components were soldered on a prototyping board (universal Through Hole and Surface Mount Schmartboard™) and connected to the load and the readout pins via a breadboard. The circuit can be seen in *Figure 48*: the red wire connects the board to channel 2 (anode), whereas the blue wire connects it to channel 1 (cathode). To test the circuit, two 4 Vpp signals with 180° phase shift were applied at input 1 of the board, and the voltage at a 2 kΩ load (i.e. the difference between channel 2 and channel 1) was probed, as shown in *Figure 49*.

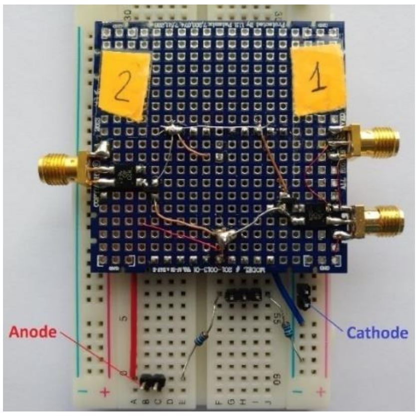

Figure 48. *First prototype of the designed circuit.*

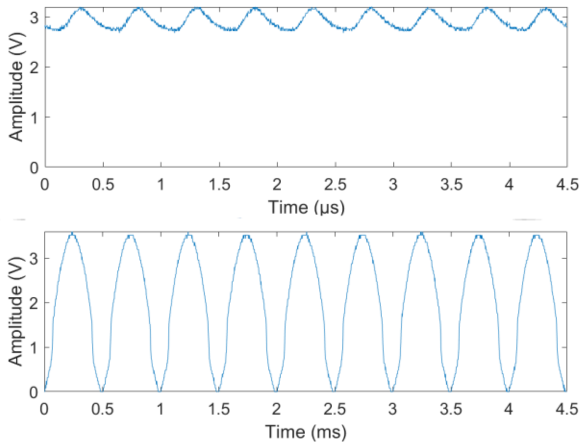

Figure 49. *Voltage at the load when testing the preliminary circuit with 1 MHz (top) and 1 KHz (bottom) input sine wave.*

It can be noticed that the signal at the output as a high offset (i.e. around 2.7 V) when using a 1 MHz input signal. This offset disappears when using a 1 kHz signal. The offset was already noticed at the output of the bridge rectifier suggesting a slow switching of the diodes, which have a junction capacitance of 250 pF each. Moreover, the pMOS was turning off already at 2 Vpp input signal; thus, a too high threshold voltage (minimum of -1 V, and maximum of -2.1 V from datasheet) for this application. For these reasons, new components were chosen and simulated. Finally, a PCB was designed in order to have a more robust circuit to interface with the available measurement setup. This is shown in *Figure 50.*

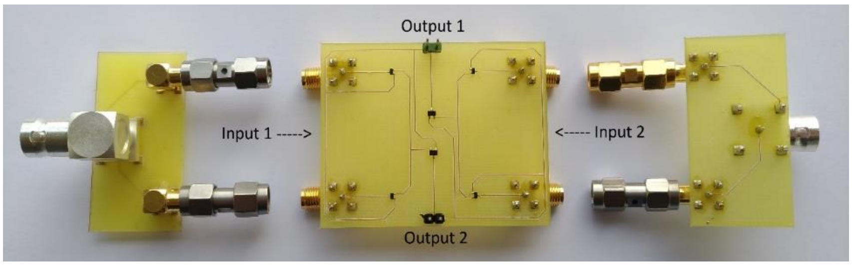

Figure 50. *Second implementation of prototype. The circuit is in the central PCB. PCBs on the sides are used to interface coaxial cables from Olympus® piezoelectric transducers to the main board.*

The circuit had to be connected to a differential sinusoidal signal coming from a waveform generator. Therefore, two coaxial cables were plugged with adapters directly to two inputs of the main board and the signal was probed from a breadboard as shown in *Figure 51.* The breadboard was used to interface the circuit with different loads. The purpose of this test was to check the general operation of the circuit before testing it with ultrasonic transducers.

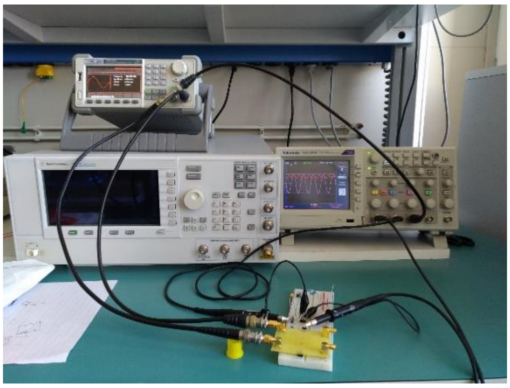

Figure 51. *Measurement setup for preliminary tests.*

The resulting waveforms were then compared with LTSpice simulations. The input signal amplitude was changed from 4 Vpp down to 1 Vpp. Moreover, both frequency of 1 MHz and 2.6 MHz were tested. In the simulator schematic, a sinusoidal voltage source was used to model the differential signal with an amplitude equal to the peak-to-peak voltage of the real differential source. The simulated circuit can be seen in *Figure 52.*

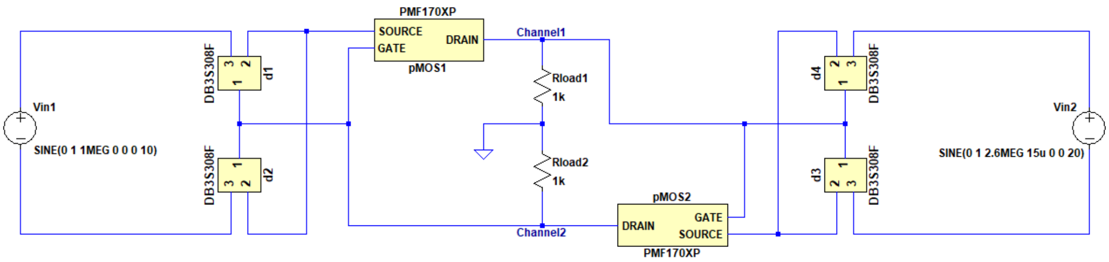

Figure 52. *LTSpice circuit schematic for simulating the preliminary tests with the final components.*

The amplitude of Vin1 and Vin2 was changed from 4 V down to 1 V. The results of measurements and simulations are illustrated in *Figure 53* for two frequencies. It can be noticed that the offset for the 1 MHz input decreased and the amplitude of the load voltage increased with respect to the previous circuit implementation. Moreover, the transistor is still operating at 2 Vpp input signal. However, the amplitude of the signal is lower than the one observed in simulation. In particular, for the 1 Vpp case the difference between simulations and measurements is more evident. This is caused by the model of the transistor used, which shows a relatively low resistance (i.e. lower than 13 kΩ) even at input voltages lower than 600 mV, thus allowing current flowing to the load at all input voltages; while, the real transistor has a minimum threshold voltage of -0.65 V and a maximum of -1.15 V. Furthermore, measurements shown that a 1.7 Vpp voltage, for both the outphased input sources, is the minimum required to completely turn on the transistor.

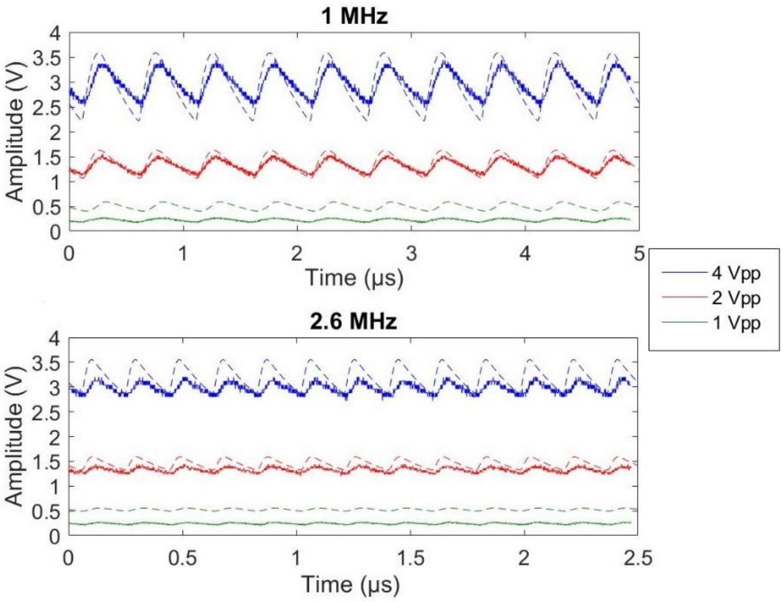

Figure 53. *Simulated (dashed lines) and measured (solid lines) load voltage with the final circuit implementation for two different input frequencies and three different input signal amplitudes.*

Finally, each of the side PCBs was used to split the signal coming from the coaxial cable of an Olympus® transducer and to use it as a differential input for the main board. When measuring the output signal, only half-wave rectification was observed at each channel due to the heavily-damping backing of the transducer. In fact, the signal coming from the outer shielding of the coaxial cable is acting as ground reference; thus, impeding the correct operation of the bridge rectifier. Therefore, the voltage across the load is half in amplitude when compared to the situation with a fully-differential signal at the input.

C. Electrodes impedance characterization

Electrochemical Impedance Spectroscopy (EIS) was performed for an array of 0.1 mm^2 PtIr electrodes (design and fabrication in [79]) in order to have a characterization of the impedance of this type of load when used in measurements (Chapter 5). The array is shown in *Figure 54*. Silicon rubber covers the metal tracks, which connect the exposed electrodes to the pads at the distal end. Wires run from the pads for connection to the EIS working electrode (WE) input or to the PCB for testing.

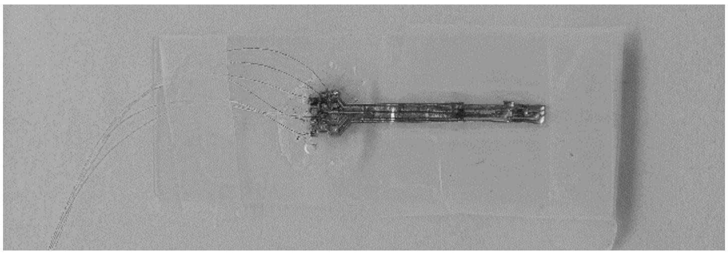

Figure 54. *Picture of PtIr electrode array used in measurements.*

A three-electrodes galvanostat was used for performing the electrochemical tests with an Ag/AgCl reference electrode (RE) and a Pt coil as counter electrode (CE). The RE, the CE, and the tested PtIr electrodes array were put in a Phosphate Buffered Saline (PBS) solution and the measurements were done inside a Faraday cage. Measurements were conducted between 10 Hz and 10 kHz with an EIS rms signal of 50 mV and 0 Vbias.

In a first test, the measured impedance was in the order of 10^5 Ω or more for all frequencies, suggesting that we could not record a signal from the WE. This can be caused by the small electrode area surrounded by hydrophobic silicon rubber; the PBS solution cannot get in contact with the metal, thus impeding a correct measurement. However, when pouring ethanol on top of the array, the wettability of the rubber material increases, thus allowing the PBS to flow towards the openings were the electrodes are exposed. The results of monopolar measurements, after ethanol wetting, are shown in *Figure 55*. The final graphs are the average of 7 measurements taken from 3 electrodes of the array.

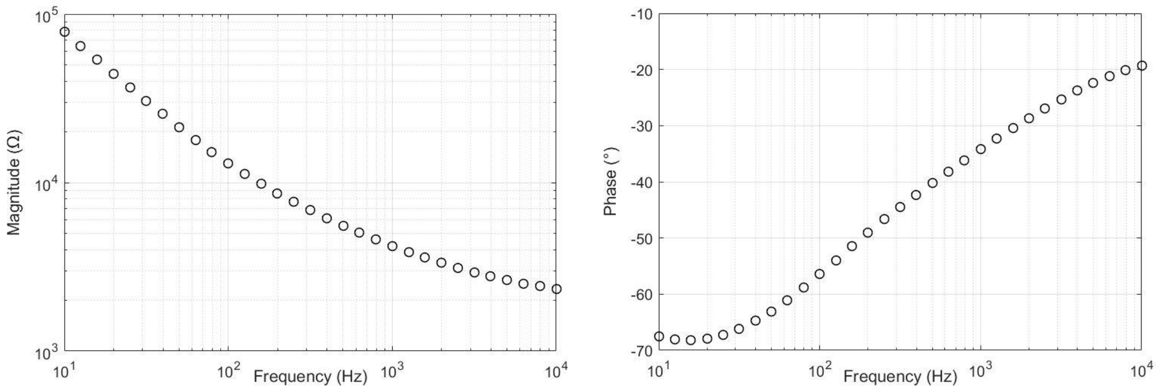

Figure 55. *Result of monopolar measurements of EIS for PtIr electrodes.*

D. Effect of acoustic echo on received signal

In a first measurement with the presented piezoelectric transducers, a significant change in the output signal was observed after 50 µs from the application of the ultrasonic burst for both the 1st and the 2nd phase of the biphasic pulse as in *Figure 56*. A DC-shift is visible both at the input of the circuit and the output. This could be explained by the interference (in this case constructive) of an ultrasonic echo received after 50 µs over the original transmitted signal.

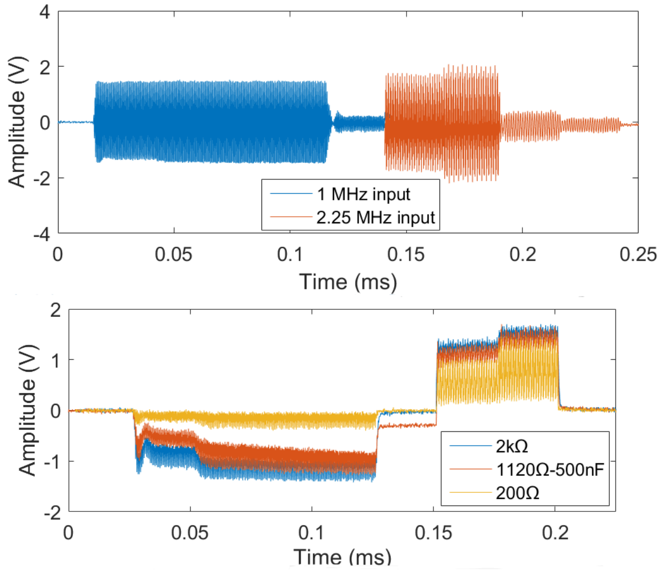

Figure 56. *Top: open-circuit voltage at the receivers. Bottom: output voltage across three different loads.*

Extra measurements were conducted to verify the presence of the echo and check the delay between the start of the excitation burst and the received signal. *Figure 57* shows the application of a 10 µs signal at 1 MHz to the transmitter, and the received signal around 20 µs afterwards. From the figure, an echo is also visible after 40 µs from the start of the first received burst. The echo is caused by the reflection of the signal from the receiver to the transmitter and back to the receiver side. This also explains why the delay time of the echo is double the one between the transmitted and the first received signal. When moving the transmitter closer or further away from the receiver, or when tilting it, the received signal changes in amplitude and the effect of the echo is stronger or weaker.

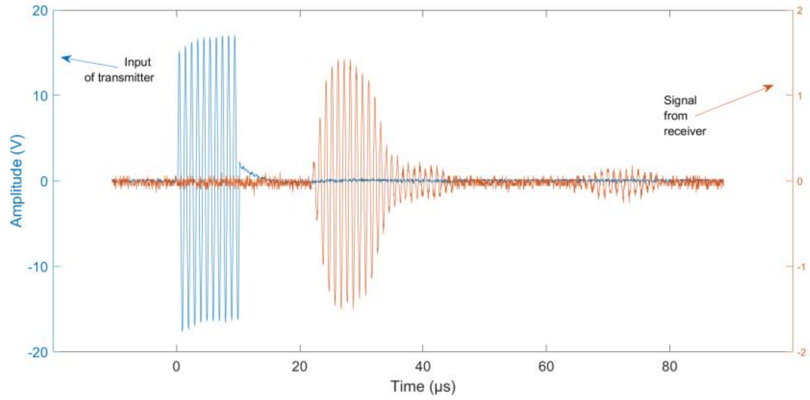

Figure 57. *Signal driving the 1 MHz transmitter and signal recorded at the receiver.*

Bibliography

[1] K. Famm, B. Litt, K. J. Tracey, E. S. Boyden, and M. Slaoui, "A jump-start for electroceuticals," *Nature*, vol. 496, no. 7444, pp. 159–161, 2013.

[2] X. Li, W. A. Serdijn, W. Zheng, Y. Tian, and B. Zhang, "The injectable neurostimulator: an emerging therapeutic device," *Trends Biotechnol.*, vol. 33, no. 7, pp. 388–394, 2015.

[3] M. Rasouli and L. S. J. Phee, "Energy sources and their development for application in medical devices," *Expert Rev. Med. Devices*, vol. 7, no. 5, pp. 693–709, 2010.

[4] D. C. Bock, A. C. Marschilok, K. J. Takeuchi, and E. S. Takeuchi, "Batteries used to power implantable biomedical devices," *Electrochim Acta.*, vol. 84, pp. 1–31, 2012.

[5] A. Kim, M. Ochoa, R. Rahimi, and B. Ziaie, "New and emerging energy sources for implantable wireless microdevices," *IEEE Access*, vol. 3, pp. 89–98, 2015.

[6] A. Ben Amar, A. B. Kouki, and H. Cao, "Power approaches for implantable medical devices," *Sensors*, vol. 15, no. 11, pp. 28889–28914, 2015.

[7] A. González, E. Goikolea, J. A. Barrena, and R. Mysyk, "Review on supercapacitors: technologies and materials," *Renew. Sustain. Energy Rev.*, vol. 58, pp. 1189–1206, 2016.

[8] J. Kerns, "What's the difference between batteries and capacitors?," 2015. [Online]. Available: http://www.machinedesign.com/batteriespower-supplies/what-s-difference-between-batteries-and-capacitors. [Accessed: 26-Jan-2018].

[9] P. Cinquin *et al.*, "A glucose biofuel cell implanted in rats," *PLoS One*, vol. 5, no. 5, p. e10476: 1-7, 2010.

[10] A. Zebda *et al.*, "Single glucose biofuel cells implanted in rats power electronic devices," *Sci. Rep.*, vol. 3, no. 1516, pp. 1–5, 2013.

[11] V. Andoralov *et al.*, "Biofuel cell based on microscale nanostructured electrodes with inductive coupling to rat brain neurons," *Sci. Rep.*, vol. 3, no. 3270, pp. 1–11, 2013.

[12] Y. Holade *et al.*, "Pacemaker activated by an abiotic biofuel cell operated in human serum solution," *Electroanalysis*, vol. 26, no. 11, pp. 2445–2457, 2014.

[13] Y. Yang, X.-J. Wei, and J. Liu, "Suitability of a thermoelectric power generator for implantable medical electronic devices," *J. Phys. D Appl. Phys.*, vol. 40, no. 18, pp. 5790–5800, 2007.

[14] P. Roberts, G. Stanley, and J. M. Morgan, "Harvesting the energy of cardiac motion to power a pacemaker," *Circulation*, vol. 118, no. 18, pp. 679–680, 2008.

[15] H. Goto, T. Sugiura, Y. Harada, and T. Kazui, "Feasibility of using the automatic generating system for quartz watches as a leadless pacemaker power source," *Med. Biol. Eng. Comput.*, vol. 37, pp. 377–380, 1999.

[16] M. A. Hannan, S. Mutashar, S. A. Samad, and A. Hussain, "Energy harvesting for the implantable biomedical devices: issues and challenges," *Biomed. Eng. Online*, vol. 13, no.

79, pp. 1–23, 2014.

[17] R. Tashiro, N. Kabei, K. Katayama, F. Tsuboi, and K. Tsuchiya, “Development of an electrostatic generator for a cardiac pacemaker that harnesses the ventricular wall motion,” *J. Artif. Organs*, vol. 5, no. 4, pp. 239–245, 2002.

[18] S. Middelhoek, S. A. Audet, and P. J. French, *Silicon Sensors*. Delft, The Netherlands, 2006.

[19] G. T. Hwang *et al.*, “Self-powered cardiac pacemaker enabled by flexible single crystalline PMN-PT piezoelectric energy harvester,” *Adv. Mater.*, vol. 26, no. 28, pp. 4880–4887, 2014.

[20] C. Dagdeviren *et al.*, “Conformal piezoelectric energy harvesting and storage from motions of the heart, lung, and diaphragm,” *PNAS*, vol. 111, no. 5, pp. 1927–1932, 2014.

[21] G. Sahara, W. Hijikata, K. Tomioka, and T. Shinshi, “Implantable power generation system utilizing muscle contractions excited by electrical stimulation.,” *Proc IMechE Part H J Eng. Med.*, vol. 230, no. 6, pp. 569–578, 2016.

[22] Z. Tang *et al.*, “Transcutaneous battery recharging by volume conduction and its circuit modeling,” in *Proc. IEEE EMBS*, New York City, USA, 2006, pp. 644–647.

[23] K. Goto, T. Nakagawa, O. Nakamura, and S. Kawata, “An implantable power supply with an optically rechargeable lithium battery,” *IEEE Trans. Biomed. Eng.*, vol. 48, no. 7, pp. 830–833, 2001.

[24] H. Liu *et al.*, “Flexible battery-less bioelectronic implants: wireless powering and manipulation by Near-Infrared light,” *Adv. Funct. Mater.*, vol. 25, no. 45, pp. 7071–7079, 2015.

[25] C. Algora and R. Peña, “Recharging the battery of implantable biomedical devices by light,” *Artif. Organs*, vol. 33, no. 10, pp. 855–860, 2009.

[26] H. Basaeri, D. B. Christensen, and S. Roundy, “A review of acoustic power transfer for bio-medical implants,” *Smart Mater. Struct.*, vol. 25, no. 12, pp. 3001–3023, 2016.

[27] A. K. RamRakhyani, S. Mirabbasi, and M. Chiao, “Design and optimization of resonance-based efficient wireless power delivery systems for biomedical implants,” *IEEE Trans. Biomed. Circuits Syst.*, vol. 5, no. 1, pp. 48–63, 2011.

[28] J. A. Von Arx and K. Najafi, “On-chip coils with integrated cores for remote inductive powering of integrated microsystems,” in *Proc. International Conference on Solid-State Sensors and Actuators*, Chicago, USA, 1997, pp. 999–1002.

[29] R. Jegadeesan, Y. X. Guo, S. C. Yen, and N. V. Thakor, “Efficient wireless power delivery and reliable telemetry for implants and safety,” in *Proc. IMWS-BIO*, Taipei, Taiwan, 2015, pp. 25–26.

[30] Y.-K. Lo *et al.*, “A 176-channel 0.5cm3 0.7g wireless implant for motor function recovery after spinal cord injury,” in *Proc. ISSCC*, San Francisco, CA, USA, 2016, pp. 382–383.

[31] Y. P. Lin *et al.*, “A battery-less, implantable neuro-electronic interface for studying the mechanisms of deep brain stimulation in rat models,” *IEEE Trans. Biomed. Circuits Syst.*, vol. 10, no. 1, pp. 98–112, 2016.

[32] A. S. Y. Poon, S. O'driscoll, and T. H. Meng, "Optimal frequency for wireless power transmission into dispersive tissue," *IEEE Trans. Antennas Propag.*, vol. 58, no. 5, pp. 1739–1750, 2010.

[33] J. Lee, J. Jang, and Y.-K. Song, "A review on wireless powering schemes for implantable microsystems in neural engineering applications," *Biomed. Eng. Lett.*, vol. 6, no. 4, pp. 205–215, 2016.

[34] E. Y. Chow, Y. Ouyang, B. Beier, W. J. Chappell, and P. P. Irazoqui, "Evaluation of cardiovascular stents as antennas for implantable wireless applications," *IEEE Trans. Microw. Theory Tech.*, vol. 57, no. 10, pp. 2523–2532, 2009.

[35] J. S. Ho *et al.*, "Wireless power transfer to deep-tissue microimplants," *PNAS*, vol. 111, no. 22, pp. 7974–7979, 2014.

[36] Q. Zhou, J. Zheng, S. Onishi, M. F. Crommie, and A. K. Zettl, "Graphene electrostatic microphone and ultrasonic radio," *PNAS*, vol. 112, no. 29, pp. 8942–8946, 2015.

[37] D. Seo *et al.*, "Wireless recording in the peripheral nervous system with ultrasonic neural dust," *Neuron*, vol. 91, no. 3, pp. 529–539, 2016.

[38] M. J. Weber, A. Bhat, T. C. Chang, J. Charthad, and A. Arbabian, "A miniaturized ultrasonically powered programmable optogenetic implant stimulator system," in *Proc. IEEE BioWireleSS*, Austin, TX, USA, 2016, pp. 12–14.

[39] J. Charthad *et al.*, "An ultrasonically powered implantable device for targeted drug delivery," in *Proc. IEEE EMBC*, Orlando, FL, USA, 2016, pp. 541–544.

[40] P. J. Larson and B. C. Towe, "Miniature ultrasonically powered wireless nerve cuff stimulator," in *Proc. IEEE EMBS NER*, Cancun, Mexico, 2011, pp. 265–268.

[41] L. Radziemski and I. R. S. Makin, "In vivo demonstration of ultrasound power delivery to charge implanted medical devices via acute and survival porcine studies," *Ultrasonics*, vol. 64, pp. 1–9, 2016.

[42] C. L. Schmidt and P. M. Skarstad, "The future of lithium and lithium-ion batteries in implantable medical devices," *J. Power Sources*, vol. 97–98, pp. 742–746, 2001.

[43] *Information for manufacturers seeking marketing clearance of diagnostic ultrasound systems and transducers*, FDA. Rockville, MD, 2008.

[44] J. Charthad, M. J. Weber, T. C. Chang, and A. Arbabian, "A mm-sized Implantable Medical Device (IMD) with ultrasonic power transfer and a hybrid bi-directional data link," *IEEE J. Solid-State Circuits*, vol. 50, no. 8, pp. 1741–1753, 2015.

[45] W. A. Serdijn, "Electronic system design and energy harvesting and power delivery." Lecture for EE4555, Delft University of Technology, 2016.

[46] P. Aqueveque and J. Barboza, "Wireless power system for charge supercapacitors as power sources for implantable devices," in *Proc. IEEE WoW*, Daejeon, South Korea, 2015, pp. 3–7.

[47] C. Meng, O. Z. Gall, and P. P. Irazoqui, "A flexible super-capacitive solid-state power supply

for miniature implantable medical devices," *Biomed. Microdevices*, vol. 15, no. 6, pp. 973–983, 2013.

[48] S. Kumar, "Atomic batteries: energy from radioactivity," *arXiv:1511.07427 [cond-mat.mtrl-sci]*, 2015. .

[49] W. H. Ko and J. Hynecek, "Implant evaluation of a nuclear power source– Betacel® battery," *IEEE Trans. Biomed. Eng.*, pp. 238–241, 1974.

[50] C. E. Ting, "Design of an EMG amplifier for a closed-loop implantable stimulator and further development of the subcutaneous electronics for experimental treatment of spinal cord injury in animal models," MSc Thesis, Dept. Med. Phys. and Bioeng., University College London, 2014.

[51] D. Fitzpatrick, "Chapter 10 - Electrical stimulation therapy for epilepsy," in *Implantable Electronic Medical Devices*, Elsevier Ldt, 2015, pp. 117–124.

[52] R. A. Bullen, T. C. Arnot, J. B. Lakeman, and F. C. Walsh, "Biofuel cells and their development," *Biosens. Bioelectron.*, vol. 21, no. 11, pp. 2015–2045, 2006.

[53] B. I. Rapoport, J. T. Kedzierski, and R. Sarpeshkar, "A glucose fuel cell for implantable brain-machine interfaces," *PLoS One*, vol. 7, no. 6, pp. 1–15, 2012.

[54] A. Ahnood *et al.*, "Diamond encapsulated photovoltaics for transdermal power delivery," *Biosens. Bioelectron.*, vol. 77, pp. 589–597, 2016.

[55] F. Mazzilli, C. Lafon, and C. Dehollain, "A 10.5 cm ultrasound link for deep implanted medical devices," *IEEE Trans. Biomed. Circuits Syst.*, vol. 8, no. 5, pp. 738–750, 2014.

[56] T. C. Chang, M. L. Wang, J. Charthad, M. J. Weber, and A. Arbabian, "A 30.5mm3 fully packaged implantable device with duplex ultrasonic data and power links achieving 95kb/s with <10-4 BER at 8.5cm depth," in *Proc. IEEE ISSCC*, San Francisco, CA, USA, 2017, pp. 460–462.

[57] D. R. Merrill, M. Bikson, and J. G. R. Jefferys, "Electrical stimulation of excitable tissue: design of efficacious and safe protocols," *J. Neurosci. Methods*, vol. 141, no. 2, pp. 171–198, 2005.

[58] M. N. van Dongen and W. A. Serdijn, "Does a coupling capacitor enhance the charge balance during neural stimulation? An empirical study," *Med. Biol. Eng. Comput.*, vol. 54, no. 1, pp. 93–101, 2016.

[59] K. Sooksood, T. Stieglitz, and M. Ortmanns, "An experimental study on passive charge balancing," *Adv. Radio Sci.*, vol. 7, pp. 197–200, 2009.

[60] K. Sooksood, T. Stieglitz, and M. Ortmanns, "An active approach for charge balancing in functional electrical stimulation," *IEEE Trans. Biomed. Circuits Syst.*, vol. 4, no. 3, pp. 162–170, 2010.

[61] M. N. van Dongen and W. A. Serdijn, "A power-efficient multichannel neural stimulator using high-frequency pulsed excitation from an unfiltered dynamic supply," *IEEE Trans. Biomed. Circuits Syst.*, vol. 10, no. 1, pp. 61–71, 2016.

[62] M. N. van Dongen, F. E. Hoebeek, S. K. E. Koekkoek, C. I. De Zeeuw, and W. A. Serdijn, “Efficacy of high frequency switched-mode stimulation in activating Purkinje cells,” *arXiv:1406.7185v1 [q-bio.NC]*, 2014.

[63] G. Erla Ólafsdóttir, “An implantable spinal cord stimulator with adaptive voltage compliance for freely moving rats,” MSc Thesis, Dept. Bioelectron., Delft University of Technology, Delft, The Netherlands, 2017.

[64] D. B. Christensen and S. Roundy, “Ultrasonically powered piezoelectric generators for bio-implantable sensors: plate versus diaphragm,” *J. Intell. Mater. Syst. Struct.*, vol. 27, no. 8, pp. 1092–1105, 2016.

[65] Panametrics-NDT™, “Ultrasonic transducers technical notes,” *Technical brochure: Olympus® NDT, Waltham, MA*. pp. 39–49, 2006.

[66] T. L. Szabo, *Diagnostic ultrasound imaging: inside out*. Hartford, Connecticut: Elsevier Academic Press, 2004.

[67] T. C. Chang, M. J. Weber, M. L. Wang, J. Charthad, B. T. Khuri-Yakub, and A. Arbabian, “Design of tunable ultrasonic receivers for efficient powering of implantable medical devices with reconfigurable power loads,” *IEEE Trans. Ultrason. Ferroelectr. Freq. Control*, vol. 63, no. 10, pp. 1554–1562, 2016.

[68] G. S. Kino, *Acoustic waves: devices, imaging, and analog signal processing*. NJ, USA: Prentice-Hall, Inc., 2000.

[69] M. O. Culjat, D. Goldenberg, P. Tewari, and R. S. Singh, “A review of tissue substitutes for ultrasound imaging,” *Ultrasound Med. Biol.*, vol. 36, no. 6, pp. 861–873, 2010.

[70] “Acoustic properties of tissue,” *Lecture for Bioe225/Rad225, Stanford*, 2016. [Online]. Available: http://web.stanford.edu/class/rad225/subdir/Class3_AcousticProperties.pdf. [Accessed: 18-Jul-2017].

[71] R. Krimholtz, D. A. Leedom, and G. L. Matthaei, “New equivalent circuits for elementary piezoelectric transducers,” *Electron. Lett.*, vol. 6, pp. 398–399, 1970.

[72] W. M. Leach, “Controlled-source analogous circuits and SPICE models for piezoelectric transducers,” *IEEE Trans. Ultrason. Ferroelectr. Freq. Control*, vol. 41, no. 1, pp. 60–66, 1994.

[73] A. Püttmer, P. Hauptmann, R. Lucklum, O. Krause, and B. Henning, “SPICE model for lossy piezoceramic transducers,” *IEEE Trans. Ultrason. Ferroelectr. Freq. Control*, vol. 44, no. 1, pp. 60–66, 1997.

[74] J. van Deventer, T. Löfqvist, and J. Delsing, “PSpice simulation of ultrasonic systems,” *IEEE Trans. Ultrason. Ferroelectr. Freq. Control*, vol. 47, no. 4, pp. 1014–1024, 2000.

[75] J. K. J. Kim, B. L. Grisso, J. K. Kim, D. S. H. D. S. Ha, and D. J. Inman, “Electrical modeling of piezoelectric ceramics for analysis and evaluation of sensory systems,” in *Proc. IEEE SAS*, Atlanta, GA, 2008, pp. 122–127.

[76] M. Prokic, *Piezoelectric transducers modeling and characterization*. Le Locle, Switzerland: MPInterconsulting, 2004.

[77] J. Malmivuo and R. Plonsey, "21. Functional Electric Stimulation," in *Bioelectromagnetism - Principles and Applications of Bioelectric and Biomagnetic Fields*, New York: Oxford University Press, 1995, pp. 493–508.

[78] D. K. Freeman *et al.*, "A sub-millimeter, inductively powered neural stimulator," *Front. Neurosci.*, vol. 11, no. 659, pp. 1–12, 2017.

[79] V. Giagka, "Flexible active electrode arrays for epidural spinal cord stimulation," Ph.D. Dissertation, Dept. Electron. and Elect. Eng., University College London, London, UK, 2015.

[80] D. Laqua, T. Suhn, K. Kring, K. Albrecht, and P. Husar, "Ultrasound communication for intelligent implants," *Biomed. Tech.*, vol. 59, no. s1, pp. 727–730, 2014.

[81] Y.-S. Luo *et al.*, "Ultrasonic power/data telemetry and neural stimulator with OOK-PM signaling," *IEEE Trans. Circuits Syst. Express Briefs*, vol. 60, no. 12, pp. 827–831, 2013.

[82] J. Charthad *et al.*, "A mm-sized wireless implantable device for electrical stimulation of peripheral nerves," *IEEE Trans. Biomed. Circuits Syst.*, vol. 12, no. 2, pp. 257–270, 2018.

[83] F. Mazzilli *et al.*, "In-vitro platform to study ultrasound as source for wireless energy transfer and communication for implanted medical devices," in *Proc. IEEE EMBS*, Buenos Aires, Argentina, 2010, pp. 3751–3754.

[84] S. Ozeri and D. Shmilovitz, "Simultaneous backward data transmission and power harvesting in an ultrasonic transcutaneous energy transfer link employing acoustically dependent electric impedance modulation," *Ultrasonics*, vol. 54, no. 7, pp. 1929–1937, 2014.

[85] X. Liu, A. Demosthenous, and N. Donaldson, "Five valuable functions of blocking capacitors in stimulators," in *Proc. IFESS*, Freiburg, Germany, 2008, pp. 322–324.

[86] F. G. S. Silva, R. N. de Lima, R. C. S. Freire, and C. Plett, "A switchless multiband impedance matching technique based on multiresonant circuits," *IEEE Trans. Circuits Syst. Express Briefs*, vol. 60, no. 7, pp. 417–421, 2013.

[87] J. P. Miller, S. Eldabe, E. Buchser, L. M. Johanek, Y. Guan, and B. Linderoth, "Parameters of spinal cord stimulation and their role in electrical charge delivery: a review," *Neuromodulation*, vol. 19, no. 4, pp. 373–384, 2016.

[88] P. H. Gorman and J. Mortimer, "The effect of stimulus parameters on the recruitment characteristics of direct nerve stimulation," *IEEE Trans. Biomed. Eng.*, vol. 30, no. 7, pp. 407–14, 1983.

[89] S. H. Song, A. Kim, and B. Ziaie, "Omnidirectional ultrasonic powering for millimeter-scale implantable devices," *IEEE Trans. Biomed. Eng.*, vol. 62, no. 11, pp. 2717–2723, 2015.

[90] Piezo Systems Inc., "Piezoceramic application data," no. 8. pp. 59–61, 2011.

[91] D. Dalecki, "Mechanical bioeffects of ultrasound," *Annu. Rev. Biomed. Eng.*, vol. 6, no. 1, pp. 229–248, 2004.

[92] R. S. Dahiya and M. Valle, "Fundamentals of piezoelectricity," in *Robotic Tactile Sensing*, Springer, 2013, pp. 195–210.